

RANS Predictions of Complex Hovering Rotor Configurations: From Micro Scale to Full Scale

James D. Baeder *
Karthikeyan Duraisamy †
Vinod K. Lakshminarayan ‡

ABSTRACT

In this work a compressible Reynolds Averaged Navier Stokes (RANS) solver is used to investigate rotor blade self-generated wake systems in hover over a wide range of Reynolds number; in order to evaluate the predictive capability of the computational approach and to understand the flow physics of the single and coaxial rotor systems. Adequately refined overset meshes, high order numerical schemes and simple robust turbulence closures are used in order to minimize numerical errors. The experimental test cases for validation are chosen to demonstrate the ability to accurately capture tip vortex formation and evolution (primary and secondary separation, peak swirl velocity, core size, and vortex trajectory) as well as surface pressure distributions and the resulting influence on rotor performance (thrust and power) all the way from full scale ($Re_{tip} > 2,000,000$) to model scale ($500,000 < Re_{tip} < 2,000,000$) to sub scale ($100,000 < Re_{tip} < 500,000$) down to micro scale ($Re_{tip} < 100,000$). For the coaxial rotor configurations, at the full and micro scales, the unsteady performance of each rotor system is studied along with the interactions that occur between the two rotor systems. At the micro scale interesting features are observed, such as leading-edge laminar separation bubbles, additional vortical structures in the turbulent trailing-edge region that lead to wake sheet instabilities, and vortex induced separation for the bottom rotor system of the coaxial configuration.

*Associate Professor, Department of Aerospace Engineering, University of Maryland, baeder@umd.edu.

†Consulting Assistant Professor, Department of Aeronautics & Astronautics, Stanford University, dkarthik@stanford.edu.

‡Research Associate, Department of Aerospace Engineering, University of Maryland, vinodkl@umd.edu.

Nomenclature

c	Chord length of the airfoil, m
C_p	Pressure coefficient
C_P	Power coefficient = $P/(\rho\pi R^2 U_{tip}^3)$ (Referred to as C_Q)
C_Q	Torque coefficient = $Q/(\rho\pi R^2 U_{tip}^2 R)$ (Equivalent to power coefficient, C_P)
$C_{Q_{bot}}$	Power coefficient of the bottom rotor
$C_{Q_{ideal}}$	Ideal power coefficient = $C_T^{3/2}/\sqrt{2}$
C_{Q_p}	Coefficient of power due to pressure forces
$C_{Q_{top}}$	Power coefficient of the top rotor
C_{Q_v}	Coefficient of power due to viscous forces
C_T	Thrust coefficient = Thrust/ $(\rho\pi R^2 U_{tip}^2)$
$C_{T_{bot}}$	Thrust coefficient of the bottom rotor
$C_{T_{top}}$	Thrust coefficient of the top rotor
$C_{T_{total}}$	Total thrust coefficient of the coaxial system
$dC_{Q_{rms}}$	Root mean square fluctuation in power coefficient
$dC_{T_{rms}}$	Root mean square fluctuation in thrust coefficient
FM	Figure of Merit = (ideal power)/(actual power)
M_{tip}	Tip Mach number
h	Distance between top and bottom rotor, m
p	Pressure, N/m^2
PL	Power Loading = Thrust/Power, N/W
q	Non-dimensionalized second invariant of the velocity gradient tensor $\frac{\partial u_i}{\partial x_j} \frac{\partial u_j}{\partial x_i}$ (normalized by tip speed and blade chord)
r	Radial location along the blade, m
R	Radius of the rotor, m

Re	Reynolds number
Re_{tip}	Tip Reynolds number
U_{tip}	Tip speed, m/s
ρ	Density, kg/m^3
ψ	Wake age, deg
ψ_{b_1}	Wake age of top rotor vortex, deg
ψ_{b_2}	Wake age of bottom rotor vortex, deg

Acronyms

BLTE	B lunt L eading and T railing E dge
SLE	S harp L eading and Blunt Trailing E dge
SLTE	S harp L eading and T railing E dge
STE	Blunt Leading and S harp T railing E dge

Introduction

The blades of a helicopter rotor constantly operate in a self-generated wake system that contains concentrated regions of intense vorticity. Under certain flight conditions such as descent and maneuvers, these vortices may directly impact the blade. These interactions typically occur before the vortices undergo any significant decay and can thus result in highly impulsive noise and vibrations. Further, in hover and low speed forward flight, multiple turns of the wake remain under the rotor at all times and the resulting induced velocity field on the rotor blades has a significant effect on the rotor thrust and power. The complexity engendered by the wake vortices makes the prediction of helicopter performance, airloads and acoustics very difficult. Successful prediction models should have enough fidelity to accurately represent the vortex formation, evolution and interaction with the blades. The associated modeling challenges arise from

a) Flow physics: Adverse pressure gradients and flow separations, laminar-turbulent transitions in the boundary layer and wake, wide range of Mach and Reynolds numbers.

b) Numerics: Typical trailing vortex core size is of the order of 0.5% of the blade radius and thus these vortices need to be convected roughly 1000 core-lengths to represent one wake revolution.

Low fidelity rotor wake models such as vortex filament/particle methods¹⁻⁶ and Eulerian vorticity transport methods (VTM)⁷ have provided useful engineering results at an affordable cost by circumventing some of the aforementioned challenges. In these methods, the blade is typically represented by a lifting line with a look-up table of sectional airfoil properties. The problem of scale in numerics is circumvented by prescribing the vortex structure (filament methods) or by assuming that the details of the order of the core radius (particle methods) or smallest cell size (VTM) are unimportant. Vorticity confinement methods,^{8,9} in which explicit source terms are added to the flow equations to counter numerical diffusion, have proved to be an interesting alternative and in many cases, have served as a very good intermediate step between vortex-based methods and Navier-Stokes solutions. In the spirit of the inviscid particle methods and the VTM - by assuming that small vortical structures do not diffuse as they convect over large distances - vorticity confinement methods are concerned with representing the global structure of the wake rather than the details of the core structure. The increased appeal of this method is that it can be invoked in a Navier-Stokes solver, thus providing a multi-fidelity approach at a much lower cost. However, the empiricism of the anti-diffusive term and its interference with the flow features in transonic/turbulent flows restricts its applicability to a wider range of flows.

There is a need for a generic and highly reliable model with low levels of empiricism if one is to address rotor problems encompassing a wide range of flow conditions (Mach and Reynolds numbers, etc.) and rotor configurations (coaxial rotors, atypical airfoil sections and blade planforms, etc.) and to evaluate local and global design modifications (active flaps, individual blade control etc.). Among the higher fidelity methods, Direct Numerical Simulations (DNS) and Large Eddy Simulations (LES) are prohibitively expensive at Reynolds numbers in the range of engineer-

ing interest, thus rendering the Reynolds Averaged Navier-Stokes (RANS) equations and hybrid RANS-LES methods as the highest fidelity alternatives for the foreseeable future. RANS based approaches themselves have inherent limitations in the form of turbulence modeling (especially for stall prediction and laminar-turbulent transition). Difficulties in controlling numerical dissipation errors in Euler and RANS calculations have also traditionally restricted their utility.

Through the use of adequately refined meshes, high order numerical schemes and simple, but robust turbulence closures, this work shows that numerical errors can indeed be kept to a minimum and accurate predictions of hovering rotor performance, vortex structure and blade vortex interactions can indeed be achieved within a generic compressible RANS framework. To evaluate the accuracy and reliability of the methodology over a wide range of flow conditions and rotor configurations, and to study the associated flow physics, the applications summarized in Table 1 will be investigated. These test cases have been logically organized to assess various aspects of the flow solution.

Computational Methodology

The computations are performed using the OVERTURNS^{10,11} flow solver, which has been under continuous development at the University of Maryland over the past decade. To allow for efficient distribution of mesh points and ease of mesh generation, structured overlapping meshes are used. Typically, body conforming meshes are used to represent the near-blade portion of the solution domain. One or more of these blade meshes are then overset inside a cylindrical background mesh. These meshes exchange information in the overlap region via interpolation. Both the blade and background meshes are refined *a priori* in regions in which the trailing vortices form and evolve, with a target spacing of at least 10 points across the estimated core size of the trailing vortex. The background meshes typically extend between to between two and three rotor radii from the blade surfaces. To account for the high induced velocities at these far-field boundaries, the point-sink boundary condition approach of Srinivasan et al.¹² is used.

The computations are performed in a time-accurate manner in the inertial frame of reference. Time integration is performed using the implicit second order accurate backwards difference

scheme with either the Lower-Upper Symmetric Gauss-Siedel (LUSGS) method¹³ or the diagonal form of implicit approximate factorization method developed by Pulliam and Chaussee¹⁴ for matrix inversion. For low Mach number configurations, time accurate preconditioning based on Turkel's¹⁵ formulation is used within a dual time stepping scheme described by Buelow et al.¹⁶ and Pandya et al.¹⁷ The inviscid spatial differencing terms are computed either using third order MUSCL scheme or using fifth order Weighted Essentially Non-Oscillatory scheme¹⁸ with Roe's upwinding and the viscous terms are computed using second order central differencing. The Spalart-Allmaras¹⁹ turbulence model is employed for the RANS closure. This one-equation model has the advantages of ease of implementation, computational efficiency and numerical stability. The production term in this eddy-viscosity model is modified²⁰ to account for the reduction of turbulence in the vortex core due to flow rotation effects.

Basic Validation Tests

Single Bladed Rotor

To assess the capability of the methodology to represent the formation and evolution of the trailing vortex over long convection distances, the experiment of Martin et al.²¹ (case 1 in Table 1) is chosen for detailed validation. In this test, a single rectangular untwisted rotor blade of aspect ratio 9.12 is operated in hover and extensive Laser Doppler Velocimetry (LDV) and Particle Image Velocimetry (PIV) measurements of the vortex velocity profiles are available along various azimuthal stations up to a wake age of one rotor revolution.

A two mesh overset system consisting of a body conforming blade mesh and a cylindrical background mesh is used for the computations. The blade mesh is of an C-O topology and is highly refined near the tip with a spacing of $0.0025c$ in the cross-stream direction (Fig. 1a). This mesh consists of 313 points in the streamwise wrap-around direction, 137 points in the spanwise direction, and 109 points in the normal direction and is overset inside a cylindrical background grid, in which a cross-stream spacing of $0.01c$ is maintained (Fig. 1b) throughout the first revolution of the trailing vortex, to ensure between 8 and 20 points across the vortex core. The dimensions

of the background grid are $187 \times 211 \times 223$ in the azimuthal, spanwise, and vertical directions, respectively.

Figure 2 shows the computed contours of streamwise vorticity at selected chordwise sections of the blade. The pressure difference between the bottom and top surfaces is seen to generate a thin cross-flow boundary layer with primarily streamwise-oriented vorticity. Upstream of the quarter-chord point, a pair of counter-rotating vortices are formed at either edge of the tip as a result of the cross-flow separation at the sharp surface edges. Immediately downstream of the quarter-chord point, as the driving pressure gradient weakens, this sheet of vorticity separates off the blade surface. The separated shear layer evolves into the primary tip vortex as a result of the roll-up caused by its self-induced velocity. Further downstream, secondary and tertiary vortices are entrained into the trailing vortex as it grows in strength with the continued roll-up of the vortex sheet. Figure 3 compares the computed velocity and vorticity with time averaged PIV measurements near the mid-chord plane. The flow-field appears qualitatively and quantitatively similar, although the secondary vortex is smeared out by the time averaging and coarse resolution of the PIV grid.

For purposes of further quantitative validation, Fig. 4 compares the computed velocity profile along a line passing through the vortex core with PIV and LDV measurements on the same test set-up at a station corresponding to three degrees of blade rotation from the trailing edge. The magnitude of peak swirl velocity predicted by the computation appears to be slightly larger than the measured values. On the other hand, away from the vortex axis, the computational predictions appear to be in striking agreement with the LDV measurements.

Figure 5 compares the computed peak swirl velocity and core radius with experiments as a function of the wake age. The third order spatial discretization is seen to perform very poorly compared to the fifth order scheme, suggesting non-optimal discretization leading to numerical dissipation. Note that the discretization uses only 7 points along the vortex core in the initial stages of the evolution, but this number increases to around 20 at later wake ages. With the fifth

For comparative purposes, all quantities are plotted on the PIV grid.

order scheme, an increase in resolution by a factor of 50% in the cross stream directions was seen to result in a $< 3\%$ increase in swirl velocity, suggesting that the mesh convergence is being approached. The rapid rate of decay of the vortex in the initial wake ages could be attributed to turbulent diffusion via the strong radial gradients of axial velocity. As these gradients reduce in magnitude very rapidly, the vortex decays at a slower rate at the later wake ages. This qualitative feature appears to be well captured by the computations.

Figure 6 shows the effect of the rotational correction in the turbulence model. As expected, the baseline SA model with no rotational correction proves to be extremely diffusive since it predicts unphysical levels of turbulent mixing in the vortical core. On comparing the third order solution with rotational correction (Fig. 5b) with the fifth order solution with no correction (Fig. 6), it is apparent that turbulence modeling uncertainties are much larger than numerical errors.

Two Bladed Rotor

To complement the single-bladed hovering rotor calculations that focused on the vortex velocity, simulations were carried out on the rectangular, untwisted two-bladed experimental setup of Caradonna and Tung²² (case 2 in Table 1). This test case was chosen since it provides detailed blade surface pressure measurements and vortex trajectory data. Figure 7 compares the sectional pressure coefficients at select spanwise locations for a collective pitch setting of 8° . The computations compare well with experiments except near the suction peak in the 80% span stations, where a discrepancy of $\sim 5\%$ is noticeable. Figure 8 shows the position of the computed vortex centers compared to the curve-fitted experimental results. The accelerated downward convection after the first pass under the blade ($\psi = 180^\circ$) is well represented. This sudden increase in downward convection is the result of the downwash from the blade and the evolving tip vortex on the first passage of the vortex. While the downward convection agrees well with experiments for all compared wake ages, the radial contraction shows disagreement in the later wake ages. Part of this discrepancy can be attributed to the computations not explicitly accounting for recirculation effects in the hover test cell.

Having gained confidence the prediction of vortex formation, evolution, trajectories and blade

pressures for simple configurations, the methodology will be applied to a wide variety of complex hovering rotor configurations in the following sections.

Micro-Scale Single Rotor

Hovering micro-scale single rotor validation is done by exploring the experimental results obtained by Ramasamy et al.^{23,24} (case 3 in Table 1) on a two-bladed hovering rotor of an aspect ratio of 4.39. The resulting solidity is 0.145. The untwisted rectangular blades used a 3.3% curvature circular arc airfoil with a thickness of 3.7% of chord. The baseline section has blunt leading and trailing edges. Experiments were also performed on sections which were different from the baseline section in the form of a sharpened leading edge (SLE) and sharpened leading and trailing edges (SLTE). Sharpening is done to a length of $0.15c$ from the leading or trailing edge. Performance data is available at various collective angles. High resolution flow visualization and particle image velocimetry (PIV) flow-field data is available for the case with a collective angle of 12° using the baseline sectional profile.

Computations are performed on rotor blades with four different sectional profiles listed below: (see Fig. 9)

1. Blunt leading and trailing edge (BLTE)
2. Sharp leading edge and blunt trailing edge (SLE)
3. Blunt leading edge and sharp trailing edge (STE)
4. Sharp leading and trailing edge (SLTE)

The modeled geometries are mostly similar to the corresponding experimental ones other than minor modifications that were made to allow simulation using a C-type airfoil grid. The geometries with sharp leading edge are modeled using a slightly rounded leading edge and those with blunt trailing edges are modeled with marginally smoothed trailing edge.

A two mesh overset system similar to that used in the previous section is used for the computations. The dimensions of the blade and background meshes were $267 \times 185 \times 99$ and $127 \times$

186 × 198, respectively. In the most refined regions, a grid spacing of 0.02 chords was used in both the radial and the vertical directions of the background grid. Along the azimuthal direction, a grid plane is spaced every 1.5°. The time-step size corresponds to 0.125° of azimuth for the fine mesh and 0.25° of azimuth for the coarse mesh calculations.

Performance Comparison

Figure 10 compares the computed performance with the experimentally measured values.²⁴ The results shown in Fig. 10 are the mean values obtained by averaging the thrust and power over one revolution. It can be seen that the computed performance for all geometries (BLTE, SLE and SLTE) shows good agreement with the experimental results. At higher thrust levels, the computed power is under-predicted by about 4 – 5% for the SLE and SLTE geometries and over-predicted by 1 – 2% for the BLTE geometry. The differences at higher thrust values can be more clearly seen in figure of merit (*FM*), see Fig. 11, where the predicted maximum *FM* is slightly higher for the sharp leading edge geometries and marginally lower for the BLTE geometry.

Comparing the performance of various geometries, it can be seen that the profile with blunt leading edge shows degraded performance at all thrust levels compared to a geometry with sharp leading edge. Also, interestingly, sharpening the trailing edge is seen to improve the performance of the geometry with blunt leading edge, but not for the geometry with sharp leading edge. The computational results also show that while the BLTE and STE geometry achieve a maximum *FM* of about 0.45 and 0.5, respectively, the sharp leading edge profiles attain a maximum *FM* greater than 0.55. The reason for the differences in performance is addressed in the following sections.

It should be noted that the performance results obtained using the fine mesh for a collective pitch setting of 12° are comparable to the coarse mesh results and, therefore, nominal convergence is being approached in the performance data.

Blade Surface Streamlines

Separation patterns on the blade surfaces are used to highlight some of the differences resulting from various geometries. Figure 12 shows the surface streamlines on the blades for the 12°

collective pitch setting. The plots shown are snapshots obtained at the end of 6 revolutions of computation on the fine mesh. The flow is attached over a majority of the blade surface for the sharp leading edge geometries, especially with blunt trailing edges. For the sharp trailing edge profile, the flow separates near the trailing edge at about 80% chord position. The inboard stations show a small portion of leading edge separation which reattaches with a fairly strong radial cross-flow. In contrast, the blunt leading edge geometries result in a leading edge separation that increases in chordwise extent towards the tip, with the flow completely separating at the tip. The reattachment downstream of the leading edge separation bubble extends to almost the same positions as for the geometries with sharp leading edge with identical trailing edge profile. It should be noted that the predicted length of separation bubble may not be very accurate in the present calculations because of the limitations of the Spalart-Allmaras turbulence model and also due to the fact that fully turbulent flow is assumed. However, the agreement in performance predictions appear to suggest that the right qualitative trends are being predicted.

Blade Pressure Distributions

The differences in the performance between the various geometries can be better understood through the surface pressure plots at selected spanwise stations. Figure 13 shows the chordwise surface pressure distribution for all four geometries at 12° collective setting at four spanwise locations. The distribution for the sharp leading edge geometries do not show much variation along the span, in stark contrast to the blunt leading edge geometries vary significantly with span, which show rapid changes in the outboard regions because of the leading edge separation. The effect of the laminar separation bubble can be seen at the 60% and 90% span locations for the blunt leading edge geometries, where the pressure distributions become relatively constant near the leading edge. At 95% span location, where the flow is completely separated, the pressure distribution on the upper surface is wavy and observed to be unsteady.

Comparing the chordwise pressure distributions for the blunt leading edge geometries with the sharp leading edge geometries having identical trailing edge profiles, it can be seen that the distributions are different near the leading edge, whereas they are comparable near the trailing

edge. The blunt leading edge geometries result in a larger suction peak which occurs at an earlier chordwise location compared to that for the sharp leading edge geometries.

Figure 14 shows the variation of surface pressure along the vertical direction at the same four spanwise locations for all four geometries at 12° collective setting. The surface pressures proceed in a clockwise manner around all geometries at all four spanwise locations, except near the suction peaks at the leading edge (at both the top and bottom for the blunt leading edge geometries). Clearly, the pressure drag for the blunt leading edge geometries are higher than that for the sharp leading edge geometries and the difference mainly occurs near the maximum z/c location which corresponds to the regions near the leading edge. The high pressure region created near the leading edge due to stagnating flow generates a significant amount of pressure drag for the blunt leading edge geometry case. A small contribution to the pressure drag also comes from the reduction in suction peak due to the leading edge laminar separation bubble. It can also be seen that the pressure drag is smaller for the blunt trailing edge geometries.

Flow-field Visualizations

Figure 15 shows streamwise vorticity contours near the blade surface for the 12° collective setting for BLTE and SLTE geometries. While the flow is smooth near the tip of the sharp leading edge geometries, numerous vortical structures can be seen on the top of the blunt leading edge geometry blades due to flow separation. It is evident that the tip vortex flow-field is extremely complicated because of the presence of a variety of secondary structures near the blade tip. The origin of these structures can be discerned from Fig. 15. While initial traces of the tip vortex can be seen slightly upstream of the quarter-chord point, secondary vortices originate from the leading edge as well as from the separation of the crossflow boundary layer. In addition to the secondary vortices, a large number of additional vortical structures are found near the trailing edge of the blade over most of the span for all cases as seen from Fig. 15; although they are much more coherent for the sharp leading edge geometries. Similar vortical structures can be seen in the experimental flow visualization²³ shown in Fig. 16. These structures are formed as a result of flow separation near the trailing edge of the blade and are seen to merge with the tip vortex a short

distance downstream of the trailing edge. These structures appear to be unique to sub scale rotors.

Evidence of the interaction between different turns of the tip vortex can be seen in Fig. 17(a), in which vorticity magnitude contours are shown along a 0° azimuthal plane of the background mesh. The tip vortex, after its first blade passage, is seen to interact with the inboard wake as well as the second blade passage, both of which introduce a strong strain-field. The experimental flow visualization²³ plotted in Fig. 17(b) is qualitatively similar to the computed flow-field and shows similar interactions.

Vortex Structure

Experimental data²³ is used to quantitatively validate the initial development and evolution of the tip vortex structure. Figures 18 and 19 compare the swirl and axial velocity profiles, respectively along a line passing through the center of the tip vortex at different wake ages. The experimental results are obtained for the baseline geometry at the 12° collective setting, therefore computational results for the BLTE geometry are used. It should be noted that the deficit of axial velocity in the core of the vortex is very large and is a result of the low Reynolds number. In general, there is good agreement between the computational and the experimental results. The peak swirl velocity is predicted correctly at all azimuth locations while the peak axial velocity deficit is over-predicted. The core radius, defined as half the distance between the peak-to-peak swirl velocity is also over-predicted. However, the rate of core growth and the rate of decay of the peak swirl velocity is predicted accurately, indicating that the inconsistency mainly arises during the formation stage of the tip vortex.

Full-Scale Coaxial Rotor

The hovering coaxial experimental setup of Harrington Rotor-2²⁵ (case 4 in table 1) is used to validate the computational predictions of coaxial rotor performance at full-scale. The aspect ratio of the blades is 8.33, resulting in an individual rotor solidity of 0.076 with rotor spacing, $H/D = 0.08$ (1.33 chords). The blade uses a NACA airfoil with a linearly varying thickness of 27.5% at $0.2R$ to 15% at R .

A six mesh system consisting of two blade meshes, two nested background meshes and two cylindrical outer background meshes is used as shown in Fig 20. The blade mesh, the nested background mesh and the outer background mesh of each rotor form an overset system. Nested background meshes are used to smoothly transfer the solution from the blade mesh to the outer background mesh. The outer background meshes communicate with each other by means of a sliding mesh interface. The solution is transferred from one mesh to the other by using a third order slope limited M3-quartic interpolation of Huynh.²⁶ Periodicity is assumed such that only one blade from each rotor system is simulated.

All the computations are performed on top and bottom rotor blade meshes having dimensions of $267 \times 155 \times 111$, the nested background meshes with $97 \times 204 \times 72$, the top rotor outer background mesh with $97 \times 270 \times 61$ points and the bottom rotor outer background mesh with $97 \times 270 \times 180$ points. In the most refined regions, the nested background mesh has a grid spacing of 0.0165 chords in the vertical direction, while the outer background mesh has a grid spacing of 0.033 chords in the same direction. In the radial direction, both the nested and outer background meshes have grid spacing of 0.02 chords in the most refined region. Along the azimuthal direction, a grid plane is spaced every 2° in the outer background mesh. For the nested background mesh, the azimuthal spacing varies from 0.3° near the blade to 2° in its outer boundaries. The time-step size corresponds to 0.125° of azimuth.

Mean Performance

Figure 21(a) compares the computed variation of mean total thrust coefficient with mean total power coefficient with the measured values. All the simulations are trimmed to within the specified criteria of 1% error. As a general trend, it is observed that as the total thrust increases, the difference between the thrust levels of the top and bottom rotors also increases. The overall performance is seen to be well predicted. At low thrust, the power is slightly over-predicted, whereas the reverse is true at higher thrust. Plotted along with the experimental data and the computed results is the curve fit using momentum theory for coaxial rotor.²⁷ The results using momentum theory also show similar trend as the CFD results.

Figure 21(b) shows the mean performance of the individual rotors. As expected, for the bottom rotor, the performance degrades significantly (about 40% increase in power for a given thrust at higher thrust levels) compared to that of a single rotor because of the influence of the wake from the top rotor. It is interesting to note that the performance of the top rotor is also slightly degraded ($\approx 15\%$ increase in power for a given thrust at higher thrust levels). Similar observations were made by Nagashima et al.⁶ in their experimental results and by Syal et al.²⁸ for the Harrington rotor-1 using a Free Vortex Method (FVM).

Unsteady Performance

Figure 22 shows the temporal variation of C_T and C_Q over one revolution for various thrust levels. Note that, when viewed from above, the top rotor rotates in an anti-clockwise fashion and the bottom rotor rotates clockwise. The azimuthal locations of the top and bottom rotors are referenced in their respective directions of rotation. Unsteadiness with a dominant 4/rev frequency (number of times a blade of one rotor encounters a blade of the other rotor in one revolution) is observed. A higher frequency variation can be seen in the form of spikes when the blades are very close to each other. Such a variation can be attributed to a *venturi* effect caused by the thickness of the blades, which leads to a reduction in pressure between the rotors. As a result, the thrust of the top rotor spikes down while the thrust of the bottom rotor shows an opposite effect. In addition there is also a loading effect created by the bound circulation of the blades is also observed. As the blades of the top and bottom rotors approach each other, each blade induces an upwash on the other blade. The upwash increases as the blades approach each other, but eventually changes in sense. Correspondingly, the forces on both the top and the bottom rotor increase as the blades approach each other, then decrease and then increase again as they move away. Further more, while the thrust and the power of the top rotor show an impulsive but phased behavior, such features are more spread out and distinct for the bottom rotor which lies in the wake of the top rotor.

Wake Trajectory

In order to separate the rotational flow regions from the highly strained regions, the iso-surfaces of the q -criterion²⁹ is shown in Fig. 23 for case 7 ($C_T = 0.007$). The plot is colored using vorticity magnitude and is obtained when the top and bottom rotors are aligned with each other. From the figure, it can be seen that the tip vortices are resolved for two blade passages. Beyond this wake-age, the background mesh becomes too coarse to accurately represent the details of the tip vortex. After passing the bottom rotor, there is a significant interaction between the tip vortices.

Flow-field Visualization

Figure 24 shows the vorticity magnitude contours for $C_T = 0.007$ in a plane that is at 30° azimuth with respect to the top rotor blade, at different instances in time. At this plane, wake age of the tip vortices trailed from the top rotor remains constant, while the wake age of those trailed from the bottom rotor increases. At the first instant, the top and the bottom rotor blades are aligned. At a later time, the bottom rotor blade can be seen to intersect the plane of interest. The vortices from the first set of rotor blades are marked T1 and B1, while the vortices from the second set are marked T2 and B2. This plot clearly shows the interaction of the vortices from the two rotors with each other and also with the inboard sheet. The various vortex-vortex and blade-vortex interactions exhibit significant unsteadiness after the first blade passage.

Micro-Scale Coaxial Rotor

Having assessed the predictive capability of OVERTURNS for micro-scale single rotor and full-scale coaxial rotors, the extension is made to the micro-scale hovering coaxial rotor case, aided by the experimental results obtained by Bohorquez et al.³⁰ (case 5 in Table 1). The aspect ratio of the blade is 4.98. The blades are of an untwisted planform with circular arc airfoil that has sharpened leading and trailing edges. The airfoil has a camber of $6\%c$ and a thickness of $2.2\%c$. The experiment was conducted at different rotor RPM and inter-rotor spacing. The collective pitch of both the top and bottom rotors were set at 16° .

The mesh system used for the computation is similar to that used for the full-scale coaxial rotor

calculation. A six mesh system consisting of two blade meshes, two nested background meshes and two cylindrical outer background meshes is used. In the most refined regions, the nested background mesh has a grid spacing of $0.02c$ in the vertical direction, while the outer background mesh has a grid spacing of $0.04c$ in the same direction. In the radial direction, both the nested and outer background meshes have grid spacing of $0.025c$ in the most refined region. Along the azimuthal direction, a grid plane is spaced every 2° in the outer background mesh. For the nested background mesh, the azimuthal spacing varies from 0.3° near the blade to 2° in its outer boundaries.

Effect of Rotor speed

Experiments were conducted for a range of RPM varying from 1900 to 2700. Correspondingly, the tip Reynolds number varied from 19,000 to 27,000 as the tip Mach number ranged from 0.0665 to 0.0945. For the RPM sweep, the rotor spacing is fixed at $h/R = 0.446$. Figure 25(a) shows the comparison between the computed and the measured variation of mean thrust with RPM for individual rotors as well as the entire system.

In the experimental test, the top and bottom rotors were torque balanced by changing the RPM of the bottom rotor, while keeping the top rotor RPM fixed. However, it was found that the difference in rotational speed required for torque balance was less than 2%. Therefore, an approximation of equal rotational speeds is reasonable. To confirm this, two sets of computations were performed; one set with identical top and bottom rotor rotational speeds and the other set that is torque trimmed using different rotational speed for the bottom rotor.

For the calculations assuming identical rotational speed for the top and bottom rotors, the total system thrust is seen to be well predicted (within 3%) at all rotational speeds. The top rotor thrust is under-predicted by approximately $< 2\%$ at all speeds whereas the bottom rotor thrust is over-predicted by approximately $< 8\%$. A better thrust prediction is obtained using the torque trimmed calculations. The over-prediction in the bottom rotor thrust reduces to within 3% and that of the entire system reduces to within 1%. However, the improvement in prediction capability is marginal compared to the increase in computational cost required for torque trimming. Consequently, all

the computations in the following sections are performed assuming identical top and bottom rotor rotational speed.

Figure 25(b) shows the comparison of mean Power Loading (PL) versus mean thrust for the total system. Clearly, the power is very well predicted for both sets of computation.

Effect of Rotor Spacing

Five different rotor spacings given by $h/R = 0.268, 0.357, 0.446, 0.536$ and 0.625 are studied. The RPM for this study is fixed at 2000. Correspondingly, the tip Reynolds number is 20,000 and tip Mach number is 0.07.

Mean Performance

Table 2 summarizes the mean values of thrust (C_T) coefficient obtained from CFD for individual rotors as well as for the entire system. Also shown is the total thrust obtained from the experiments. It can be seen that the computed top and bottom rotor thrusts show opposite trends as the rotor spacing increases. While the top rotor thrust increases with the rotor spacing, the bottom rotor thrust decreases as the rotor separation increases. Both the rotor thrusts approach a constant value at very large rotor spacing. Because of the opposing trends in the top and bottom rotor thrusts, the total thrust of the system is seen to remain fairly constant with the rotor spacing, apart from the marginal increase in value at smaller rotor separation distances. Similar trends can be seen in the experimental results. Table 2 also shows the ratio of the top rotor thrust to the total thrust. Top rotor contributes to about 55% of the total value at smaller rotor spacing and increases to about 58% at the largest rotor separation. These ratios are very similar to those observed for the full-scale coaxial rotor.

Unsteady Performance

A measure of the unsteadiness in thrust is the root mean square value of the temporal variations and this is summarized in Table 3. For the top rotor, the absolute value of the fluctuation decreases with increasing rotor spacing, however surprisingly, for the bottom rotor, the absolute fluctuations initially decrease and then increase again as the rotor separation increases. The reasons behind this

behavior will be addressed below. The fluctuations of the integrated quantities of the whole system follows a similar trend as that of the bottom rotor. In general, a 3 – 8% fluctuation is noticeable in all integrated quantities, which could be significant for vibration and acoustic characteristics.

Figures 26 show the temporal variation of C_T over one revolution for all rotor spacings. As seen for the full-scale coaxial rotor, the figure clearly shows the unsteadiness with a dominant 4/rev frequency. A high frequency variation is seen at all times due to shedding near the trailing edge, as observed in the single micro-rotor (Fig. 15). The higher frequency variation seen in the full-scale coaxial rotor near the blade passage due to thickness effect is not as prominent because the airfoil sections are relatively thin.

For the bottom rotor, the unsteadiness is not seen to follow any particular trend compared to the the rotor spacing, which is in contrast to the full-scale system. The reason for the differences can be understood by comparing the temporal variation of thrust and power for the bottom rotor of the micro-scale system along with that of the full-scale system (Fig. 22(b) and (d)). All the plots show two peaks (apart from the peak due to thickness effect on the full-scale system). The peak which occurs close to the blade-passage is due to the loading effect and the other peak occurs when the vortex from the top rotor impinges upon the bottom rotor (note that the peaks coincide in some plots). Clearly, in contrast to the full-scale system, the peak due to vortex impingement is more prominent and at times larger than the peak due to loading effect for the micro-scale rotor. This suggests that the wake effect for the micro-scale system is comparable to the loading effect when the rotor spacing is large. Therefore, the unsteadiness in the integrated quantities for the bottom rotor of the micro-scale coaxial system does not necessarily decrease with increased rotor spacing. On the other hand, because of the decrease in the dominant loading effect for the full-scale systems, an increase in rotor spacing almost always results in a decrease in the unsteadiness of the bottom rotor forces. In Fig. 26, the peak due to vortex impingement is seen to move to a later azimuth as the rotor spacing increases, as it takes longer to convect vertically downwards. The peak due to vortex impingement for $h/R = 0.268, 0.357, 0.446, 0.536$ and 0.625 respectively occur at the $76^\circ, 2^\circ, 22^\circ, 48^\circ$ and 68° azimuth locations. For $h/R = 0.268$ and $h/R = 0.625$, the peaks

due to vortex impingement and the loading effect are almost coincident, whereas for $h/R = 0.446$, the peaks are farthest apart. Clearly, the unsteadiness in the forces of the bottom rotor is smallest for $h/R = 0.446$, indicating that the phasing of the vortex impingement upon the bottom rotor can play a significant role in reducing unsteadiness for the micro-scale coaxial systems.

Flow-field Visualization

Figure 27 shows the vorticity magnitude contours for $h/R = 0.268$ in a plane that is fixed with respect to the bottom rotor blade, at different instances in time. In this plane, the wake ages of the tip vortices trailed from the bottom rotor remain constant (0° , 180° , 360° etc.), while the wake ages of those trailed from the top rotor increase. At the earliest shown instant, the top and the bottom rotor blades are aligned. The vortices from the first top and bottom rotor blades are marked T1 and B1, respectively, while the vortices from the second top and bottom rotor blades are marked T2 and B2, respectively. The plot clearly shows the interaction of the vortices from the two rotors with each other and also with the inboard sheet. The impingement of the top rotor vortex upon the bottom rotor occurs just before Fig. 27(f) which corresponds to 156° wake-age of the top rotor vortex (78° azimuth in time). Note that for this rotor spacing, a peak in integrated quantities of the bottom rotor occurred at an azimuth of 76° and this plot confirms that the peak is indeed due to the vortex impingement. Similar conclusions can be made from the rotor spacing of $h/R = 0.446$ and $h/R = 0.625$.

Conclusion

A compressible Reynolds Averaged Navier Stokes (RANS) solver was applied to simulate the tip vortex formation and evolution in hover as well as the resulting performance from the micro scale all the way up to full scale for comparison with experimental data. In all cases, the rotor wake structure was well preserved for several blade passages. Performance predictions were very good for all of the rotor systems examined.

Several unique features were observed for the single rotor system as they approached the micro scale: leading edge separation bubbles, additional vortical structures in the turbulent trailing-edge

region that lead to wake sheet instabilities, and turbulent separation towards the tip of the blade for some of the configurations at modest collectives. The peak swirl velocity was well predicted at all wake ages, whereas the axial deficit along the vortex center and the vortex core radius were overpredicted and the peak vorticity was under-predicted at all wake ages.

For the full scale coaxial rotor systems the bottom rotor was shown to have degraded performance due to the influence of the top rotor wake. Interestingly, the top rotor also showed slight degradation due to the influence of the bottom rotor. The top rotor tended to contribute on the order of 55% of the total thrust. The computed performance data showed that the flow-field was highly unsteady with a dominant N_b/rev frequency. As a result of the finite thickness of the blade surfaces, the integrated thrust and power showed an impulsive behavior when the blades of the top and bottom rotor were aligned. Additional impulsiveness was generated due to the blade loading. For the bottom rotor, the added influence of the top rotor wake makes the features more spread out and distinct. Additionally, the wake of the top rotor was observed to contract at a faster rate and convect vertically downward at a faster rate due to the interactions between the rotor wake systems. Significant wandering was observed at later wake ages as the tip vortices from the two rotor systems entered into a leap-frogging state.

Although the model scale rotor system exhibited the same features as for the full scale system, some other features became apparent as well: there was additional high frequency oscillations for the top and bottom rotor systems due to the instabilities in the wake sheet. Furthermore, the rotor wake interaction with the bottom rotor was more complicated with instances of highly three-dimensional shedding outboard of the interaction on the upper surface and two-dimensional shedding inboard on the lower surface.

Acknowledgments

The authors wish to acknowledge that the micro-scale single rotor work was funded by the Army Research Office Contract MURI ARMY-W911NF0410176 and the full-scale coaxial work was funded by the National Rotorcraft Technology Center / Center for Rotorcraft Innovation under the "Detailed CFD Simulations of Coaxial Rotor Systems" project (2008-B-11-01.2A9). The

micro-scale coaxial work is supported by Army's MAST-CTA center on Microsystem Mechanics, Technical Monitor Dr. Joseph Mait.

REFERENCES

¹Leishman, J. G., and Ananthan, S., "Aerodynamic Optimization of a Coaxial Proprotor," American Helicopter Society 62nd Annual Forum Proceedings, Phoenix, AZ, May 9–11, 2006.

²Leishman, J. G., Bhagwat, M. J., and Bagai, A., "Free- Vortex Filament Methods for the Analysis of Helicopter Rotor Wakes," *Journal of Aircraft*, Vol. 39, (5), September-October, 2002, pp. 759–775.

³Andrew, M. J., "Coaxial Rotor Aerodynamics," Ph.D. Dissertation, Southampton University, England, 1981.

⁴Bagai, A., and Leishman J. G., "Free-Wake Analysis of Tandem, Tilt-Rotor and Coaxial Rotor Configurations," *Journal of the American Helicopter Society*, Vol. 41, (3), July 1996, pp. 196–207.

⁵Griffiths, D. A., and Leishman, J. G., "A Study of Dual-Rotor Interference and Ground Effect Using a Free-Vortex Wake Model," American Helicopter Society 58th Annual Forum Proceedings, Montreal, Canada, June 11–13, 2002.

⁶Nagashima, T., and Nakanishi, K., "Optimum Performance and Wake Geometry of Coaxial Rotor in Hover," Paper No. 41, Seventh European Rotorcraft and Powered Lift Aircraft Forum, Garmisch-Partenkirchen, Federal Republic of Germany, 1981.

⁷Brown, R. E., "Rotor Wake Modeling for Flight Dynamic Simulation of Helicopters," *AIAA Journal*, Vol. 38, (1), January 2000, pp. 57–63.

⁸Steinhoff, J. and Underhill, D., "Modification of the Euler Equations for "Vorticity Confinement: Application to the computation of interacting vortex rings," *Physics of Fluids*, Vol. 6, (8), August 1994, pp. 2738–2744.

⁹Steinhoff, J., Yonghu, W., and Lesong, W., "Efficient Computation of Separating High

Reynolds Number Incompressible Flows Using Vorticity Confinement,” AIAA Paper 1999-3316, 14th Computational Fluid Dynamics Conference, Norfolk, VA, June 28–July 1 1999.

¹⁰Duraisamy, K., “Studies in Tip Vortex Formation, Evolution and Control,” Ph.D. Dissertation, Department of Aerospace Engineering, University of Maryland at College Park, 2005.

¹¹Lakshminarayan, V. K., “Computational Investigation of Micro-Scale Coaxial Rotor Aerodynamics in Hover,” Ph.D. Dissertation, Department of Aerospace Engineering, University of Maryland at College Park, 2009.

¹²Srinivasan, G. R., and Baeder, J. D., “TURNS: A Free-wake Euler/ Navier-Stokes Numerical method for Helicopter Rotors,” *AIAA Journal*, Vol. 31, (5), May 1993, pp. 959–962.

¹³Yoon, S., and Jameson, A., “Lower-Upper Symmetric-Gauss-Seidel Method for the Euler and Navier-stokes Equations,” *AIAA Journal*, Vol. 26, (9), September 1988, pp. 1025–1026.

¹⁴Pulliam, T. H., and Chaussee, D. S., “A Diagonal Form of an Implicit Approximate Factorization Algorithm,” *Journal of Computational Physics*, Vol. 39, (2), February 1981, pp. 347–363.

¹⁵Turkel, E., “Preconditioning Techniques in Computational Fluid Dynamics,” *Annual Review of Fluid Mechanics*, Vol. 31, January 1999, pp. 385-416.

¹⁶Buelow, P. E. O., Schwer, D. A., Feng, J., and Merkle, C. L., “A Preconditioned Dual-Time, Diagonalized ADI scheme for Unsteady Computations,” AIAA paper 1997-2101, 13th AIAA Computational Fluid Dynamics Conference, Snowmass Village, CO, June 29–July 2, 1997.

¹⁷Pandya, S. A., Venkateswaran, S., and Pulliam, T. H., “Implementation of Preconditioned Dual-Time Procedures in OVERFLOW,” AIAA paper 2003-0072, 41st AIAA Aerospace Sciences Meeting and Exhibit, Reno, NV, January 6–9, 2003.

¹⁸Jiang, G.-S., and Shu, C.-W., “Efficient implementation of weighted ENO schemes,” *Journal of Computational Physics*, Vol. 126, (1), June 1996, pp. 202–228.

¹⁹Spalart, P.R., and Allmaras, S.R., “A One-equation Turbulence Model for Aerodynamic Flows,” AIAA Paper 1992-0439, 30th AIAA Aerospace Sciences Meeting and Exhibit, Reno, NV, January 6–9, 1992.

²⁰Dacles-Mariani, J., Zilliac, G. G., Chow, J. S., and Bradshaw, P., “Numerical/ Experimental Study of a Wing tip Vortex in the Near Field,” *AIAA Journal*, Vol. 33, (9), September 1995, pp. 1561–1568.

²¹Martin, P. B., Pugilese, G. J., and Leishman, J. G., “High Resolution Trailing Vortex Measurements in the Wake of a Hovering Rotor,” *Journal of the American Helicopter Society*, Vol. 48, (1), January 2003, pp. 39–52.

²²Caradonna, F. X., and Tung, C., “Experimental and Analytical Studies of a Model Helicopter Rotor in Hover,” NASA-TM-81232, September 1981.

²³Ramasamy, M., Leishman, J. G., and Lee, T. E., “Flow Field of a Rotating Wing MAV,” *Journal of Aircraft*, Vol. 44, (4), July 2007, pp. 1236-1244.

²⁴Ramasamy, M., Johnson, B., and Leishman, J. G., “Understanding the Aerodynamic Efficiency of a Hovering Micro-Rotor,” *Journal of the American Helicopter Society*, Vol. 53, (4), October 2008, pp. 412–428.

²⁵Harrington, R. D., “Full-Scale-Tunnel Investigation of the Static-Thrust Performance of a Coaxial Helicopter Rotor,” NACA-TN-2318, March 1951.

²⁶Huynh, H. T., “Accurate Monotone Cubic Interpolation,” *SIAM Journal of Numerical Analysis*, Vol. 30, (1), February 1993, pp. 57–100.

²⁷Leishman, J. G., and Syal, M., “Figure of Merit Definition for Coaxial Rotors,” *Journal of the American Helicopter Society*, Vol. 53, (3), July 2008, pp. 290–300.

²⁸Syal, M., “Contributions to the Aerodynamic Optimization of a Coaxial Rotor system,” Master’s Thesis, Department of Aerospace Engineering, University of Maryland at College Park, 2008.

²⁹Jeong, J. and Hussain, F., “On the Identification of a Vortex,” *Journal of Fluid Mechanics*, Vol. 285, 1995, pp. 69–94.

³⁰Bohorquez, F., “Rotor Hover Performance and System Design of an Efficient Coaxial Rotary Wing Micro Air Vehicle,” Ph.D dissertation, Department of Aerospace Engineering, University of Maryland at College Park, 2007.

List of Tables

1	Summary of baseline validation sets. Note: Cases 4 and 5 are coaxial rotor configurations at full scale and micro scale, respectively	26
2	Computed mean thrust coefficient for micro-scale coaxial system.	27
3	Computed RMS fluctuation of thrust coefficient for micro-scale coaxial system. . .	28

Table 1: Summary of baseline validation sets. Note: Cases 4 and 5 are coaxial rotor configurations at full scale and micro scale, respectively

Case	Radius (m)	Blades	Airfoils	M_{tip}	Re_{tip}	Expt. Ref.	Mesh size
1	0.41	1 × 1	NACA 2415	0.26	2.7×10^5	21	6 M
2	1.14	1 × 2	NACA 0012	0.44	2.0×10^6	22	8 M
3	0.086	1 × 2	3.7% thick Circ. arc	0.08	3.2×10^4	23	9.6 M
4	3.81	2 × 2	Various NACA	0.35	3.5×10^6	25	18.3 M
5	0.112	2 × 2	2.2% thick Circ. arc	0.07	2.0×10^4	30	6.6 M

Table 2: Computed mean thrust coefficient for micro-scale coaxial system.

h/R	$C_{T_{top}}$	$C_{T_{bot}}$	$C_{T_{total}}$	$C_{T_{top}}/C_{T_{total}}$	$C_{T_{total}}$ (Expt. ³⁰)
0.268	0.0199	0.0163	0.0362	0.55	0.0349
0.357	0.0205	0.0158	0.0363	0.56	0.0349
0.446	0.0208	0.0157	0.0365	0.57	0.0350
0.536	0.0210	0.0155	0.0365	0.58	0.0350
0.625	0.0212	0.0153	0.0365	0.58	0.0350

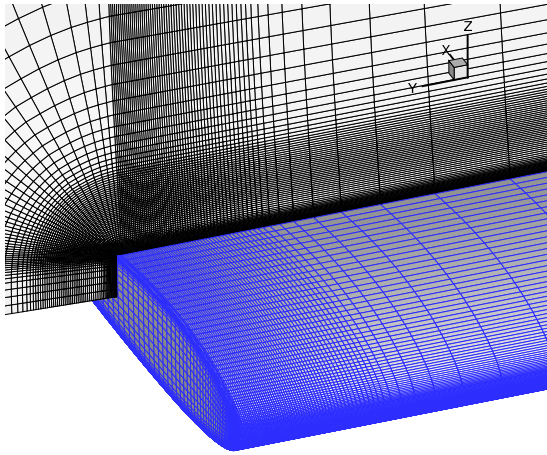
Table 3: Computed RMS fluctuation of thrust coefficient for micro-scale coaxial system.

h/R	$dC_{T_{rms}}$ (top rotor)	% fluctuation	$dC_{T_{rms}}$ (bottom rotor)	% fluctuation	$dC_{T_{rms}}$ (total)	% fluctuation
0.268	0.00105	5.28%	0.00164	10.06%	0.00237	6.55%
0.357	0.00065	3.17%	0.00074	4.68%	0.00074	2.04%
0.446	0.00040	1.92%	0.00057	3.63%	0.00088	2.41%
0.536	0.00036	1.71%	0.00091	5.87%	0.00120	3.29%
0.625	0.00024	1.13%	0.00105	6.86%	0.00117	3.21%

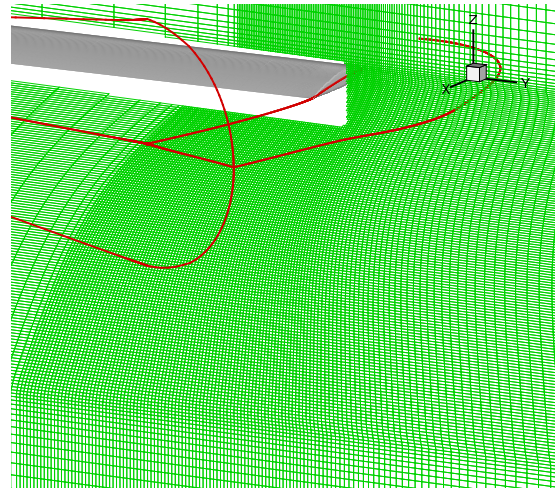
List of Figures

1	Mesh used for single bladed rotor validations	31
2	Streamwise vorticity contours in the single bladed rotor	32
3	Vorticity contours and velocity vectors near mid-chord location for single bladed rotor	33
4	Comparison of vortex velocity 0.5 chords downstream of trailing edge	34
5	Comparison of numerical schemes for vortex evolution in single bladed rotor	35
6	Effect of rotational correction in turbulence model for vortex evolution in single bladed rotor	36
7	Comparison of computed pressure coefficient (lines) with experiments (symbols) for two bladed hovering rotor	37
8	Comparison of computed vortex center locations (solid lines) with curve-fitted experimental results (dashed lines) of two bladed rotor	38
9	Computational sectional profiles for micro-scale single rotor.	39
10	Performance Comparison (C_T vs C_Q) with experimental data ²⁴ for micro-scale single rotor.	40
11	Performance Comparison (FM vs C_T) with experimental data ²⁴ for micro-scale single rotor.	41
12	Blade surface streamlines for micro-scale single rotor, 12° collective setting.	42
13	Blade pressure distribution at different spanwise location for micro-scale single rotor, 12° collective setting.	43
14	Blade pressure distribution at different spanwise location for micro-scale single rotor, 12° collective setting.	44
15	Contours of streamwise vorticity (normalized by tip speed and blade chord) for micro-scale single rotor, 12° collective setting.	45
16	Experimental flow visualization (Ref. 23).	46
17	Flow-field comparison for micro-scale single rotor.	47
18	Vortex swirl velocity profile (non-dimensionalized by tip speed) comparison between computational BLTE geometry and experimental baseline geometry ²³ of micro-scale single rotor, 12° collective setting.	48
19	Vortex axial velocity profile (non-dimensionalized by tip speed) comparison between computational BLTE geometry and experimental baseline geometry ²³ for micro-scale single rotor, 12° collective setting.	49
20	Computational mesh for full-scale coaxial rotor system.	50
21	Comparison of performance with experimental data ²⁵ for full-scale coaxial system.	51
22	Temporal variation of C_T and C_Q for the top and bottom rotors over one revolution for various thrust levels for full-scale coaxial system.	52
23	Iso-surfaces of the second invariant of the velocity gradient tensor colored by vorticity magnitude for full-scale coaxial system when the blades are aligned, case 7 ($C_T = 0.007$).	53
24	Vorticity magnitude contours (normalized by tip speed and blade chord) in a plane that is at 30° azimuth from the top rotor blade at different instances in time for full-scale coaxial system at $C_T = 0.007$	54

25	Performance comparison with experimental data ³⁰ at different RPM for micro-scale coaxial rotor.	55
26	Temporal variation of C_T of the top and bottom rotors over one revolution for various rotor spacing for micro-scale coaxial system.	56
27	Vorticity magnitude contours in the plane of the bottom rotor blade at different instances in time for micro-scale coaxial system, $h/R = 0.268$	57



a) Sample chordwise section of blade mesh



b) Sample azimuthal section (with hole) of background mesh. Blade mesh boundaries are shown as lines

Figure 1: Mesh used for single bladed rotor validations

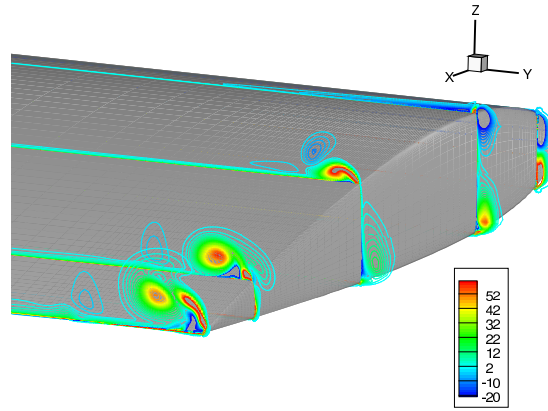
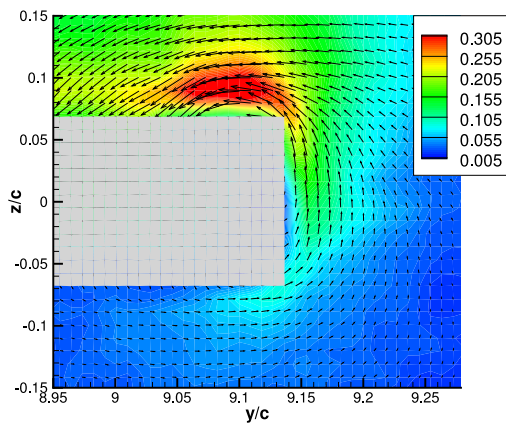
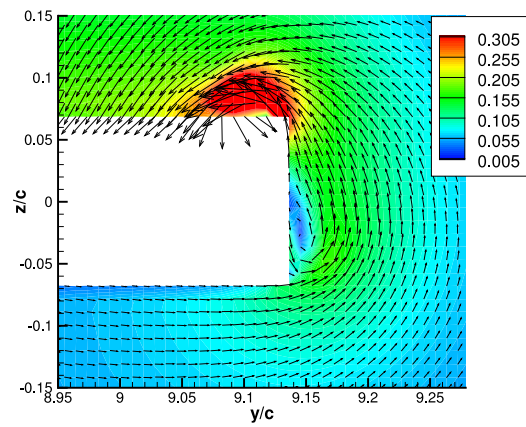


Figure 2: Streamwise vorticity contours in the single bladed rotor



a) PIV measurements



b) RANS computations

Figure 3: Vorticity contours and velocity vectors near mid-chord location for single bladed rotor

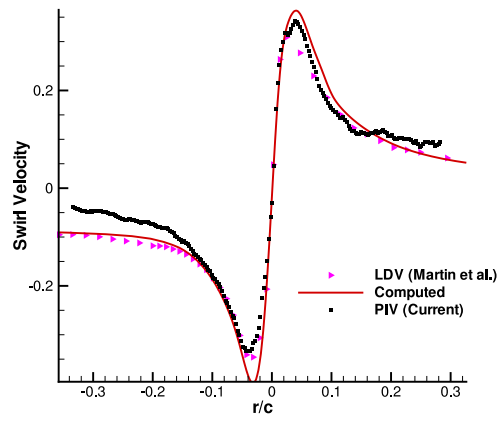


Figure 4: Comparison of vortex velocity 0.5 chords downstream of trailing edge

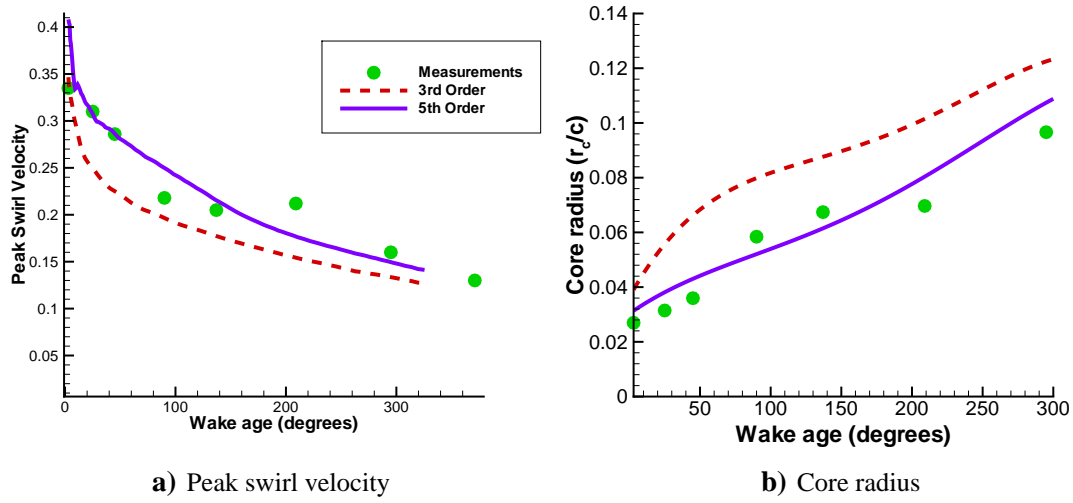


Figure 5: Comparison of numerical schemes for vortex evolution in single bladed rotor

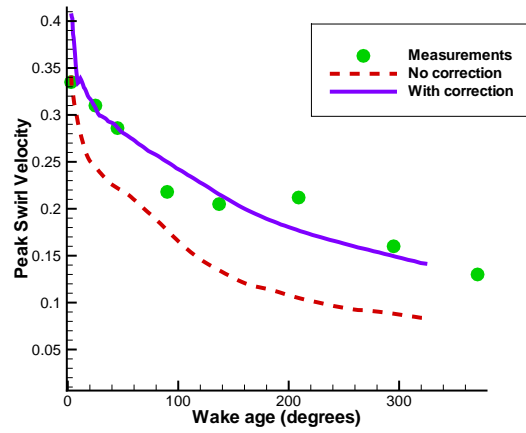
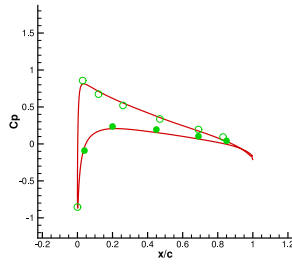
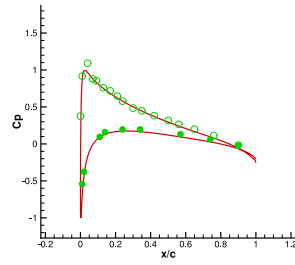


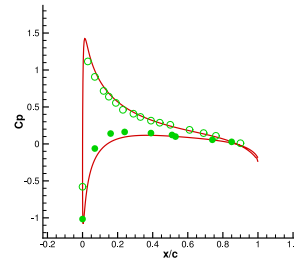
Figure 6: Effect of rotational correction in turbulence model for vortex evolution in single bladed rotor



a) 50% span



b) 80% span



c) 96% span

Figure 7: Comparison of computed pressure coefficient (lines) with experiments (symbols) for two bladed hovering rotor

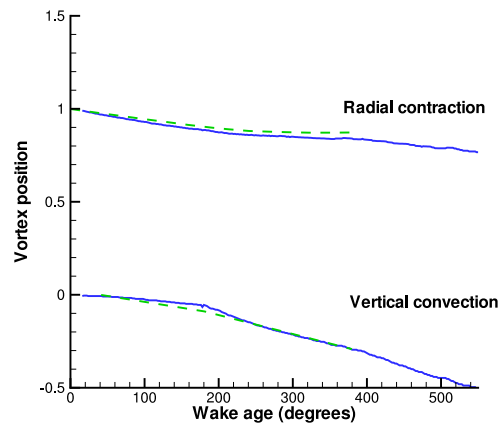


Figure 8: Comparison of computed vortex center locations (solid lines) with curve-fitted experimental results (dashed lines) of two bladed rotor

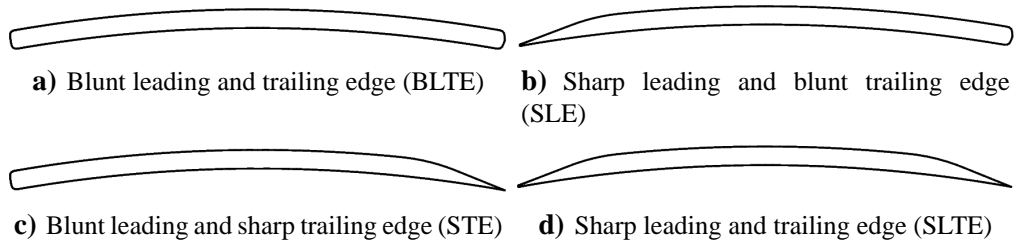
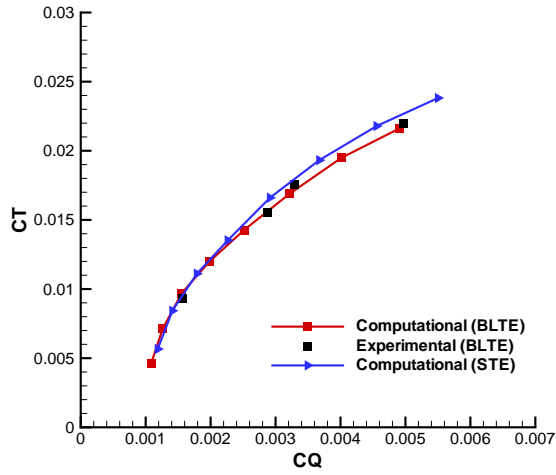
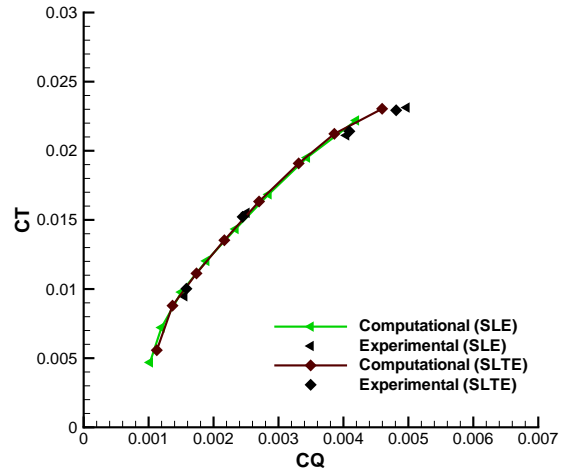


Figure 9: Computational sectional profiles for micro-scale single rotor.



a) C_T vs C_Q



b) FM vs C_T

Figure 10: Performance Comparison (C_T vs C_Q) with experimental data²⁴ for micro-scale single rotor.

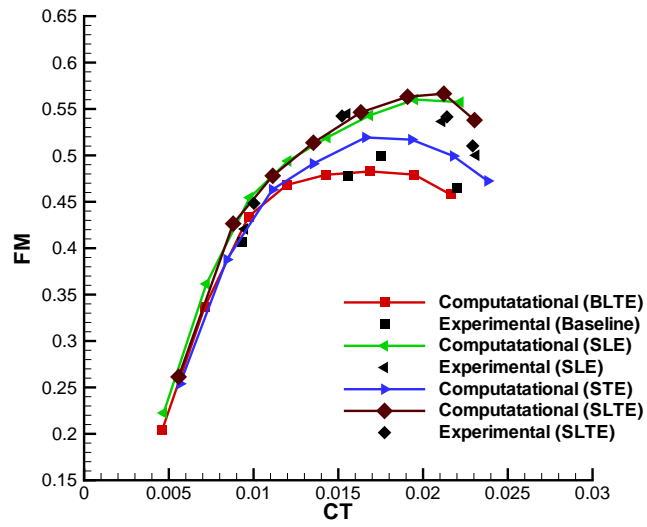


Figure 11: Performance Comparison (FM vs C_T) with experimental data²⁴ for micro-scale single rotor.

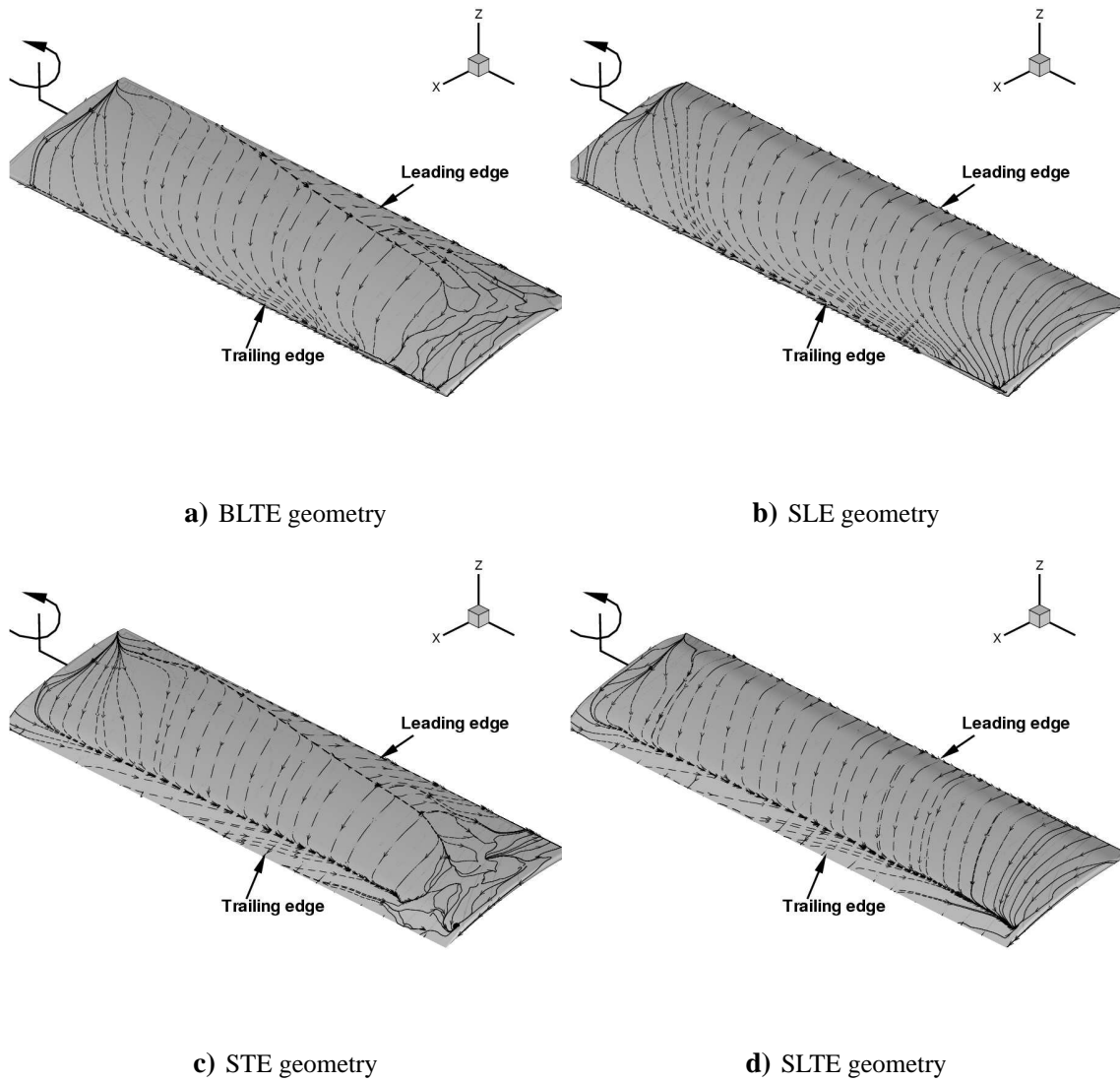
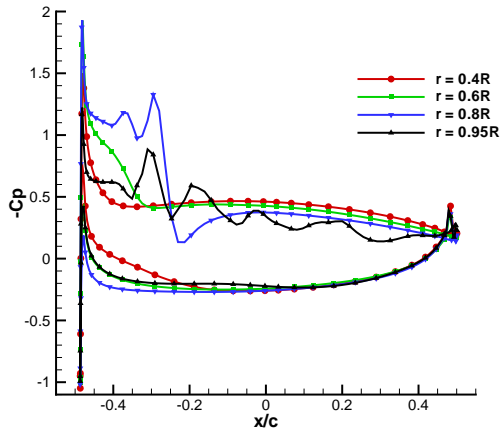
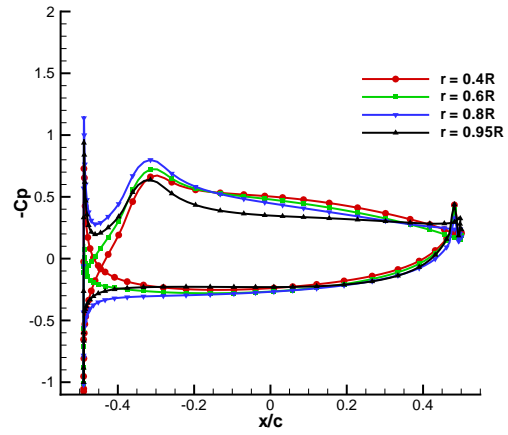


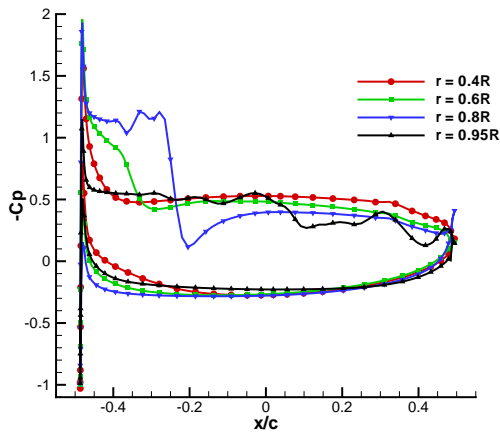
Figure 12: Blade surface streamlines for micro-scale single rotor, 12° collective setting.



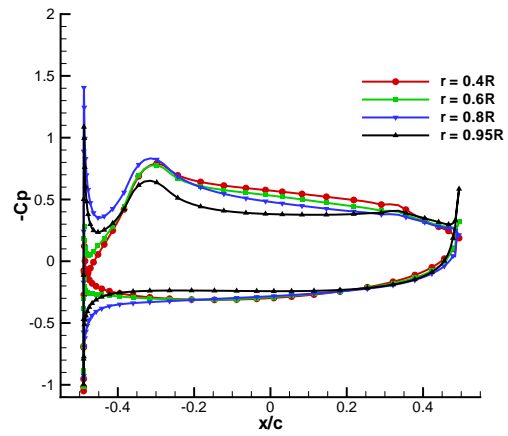
a) BLTE geometry



b) SLE geometry

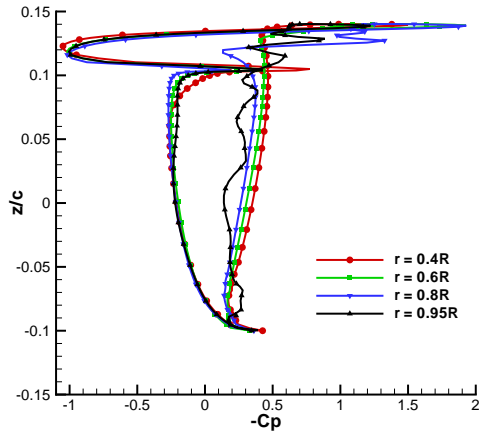


c) STE geometry

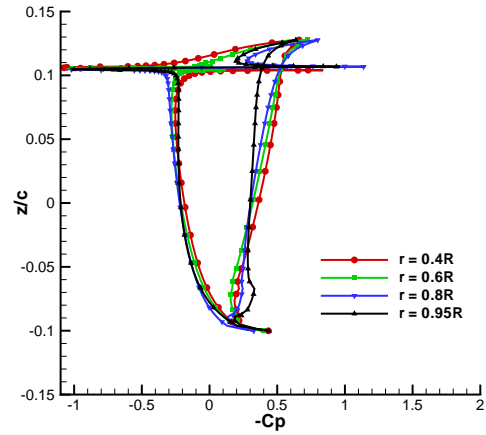


d) SLTE geometry

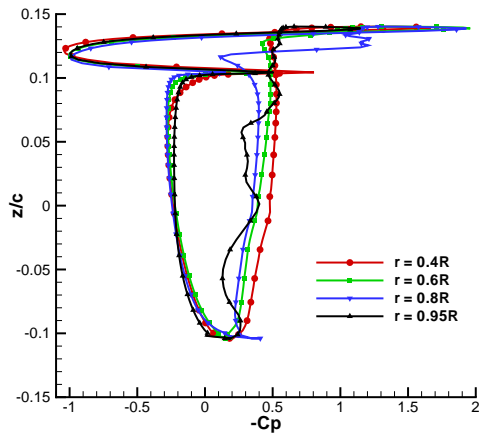
Figure 13: Blade pressure distribution at different spanwise location for micro-scale single rotor, 12° collective setting.



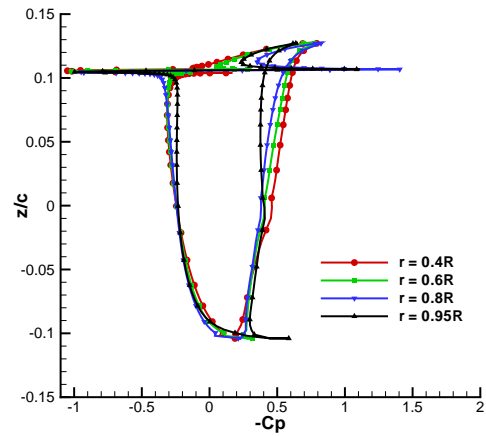
a) BLTE geometry



b) SLE geometry



c) STE geometry



d) SLTE geometry

Figure 14: Blade pressure distribution at different spanwise location for micro-scale single rotor, 12° collective setting.

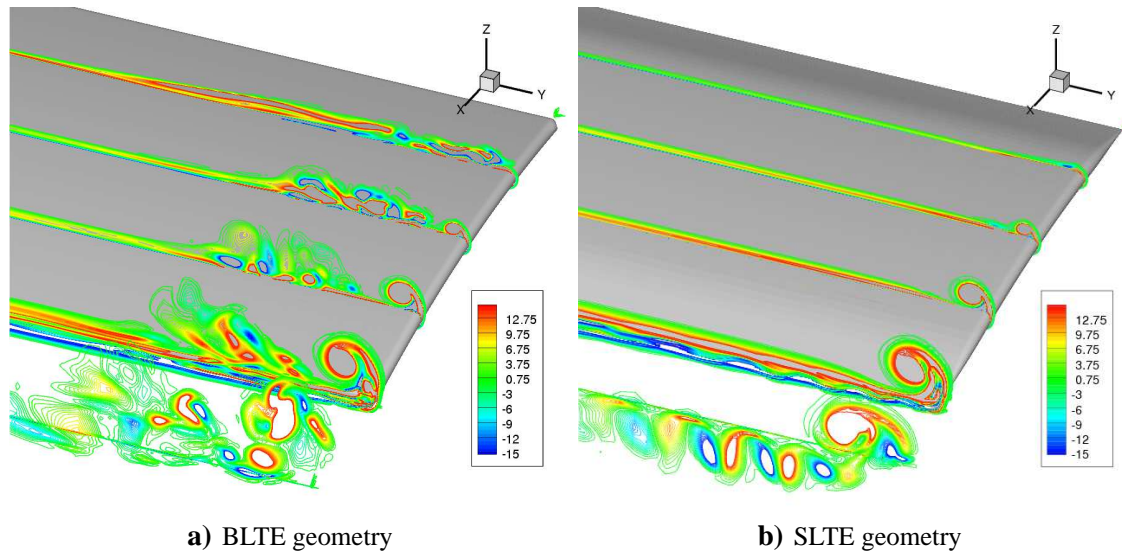


Figure 15: Contours of streamwise vorticity (normalized by tip speed and blade chord) for micro-scale single rotor, 12° collective setting.

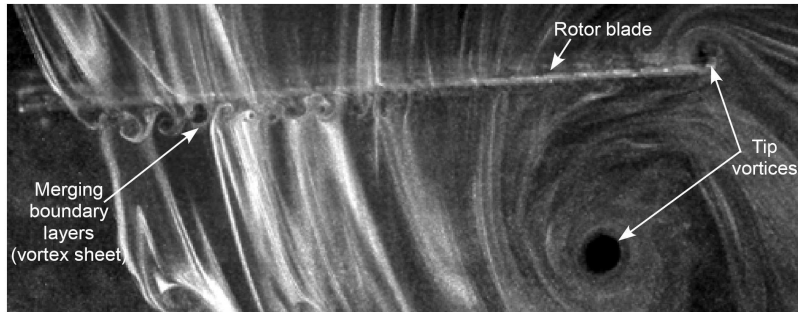
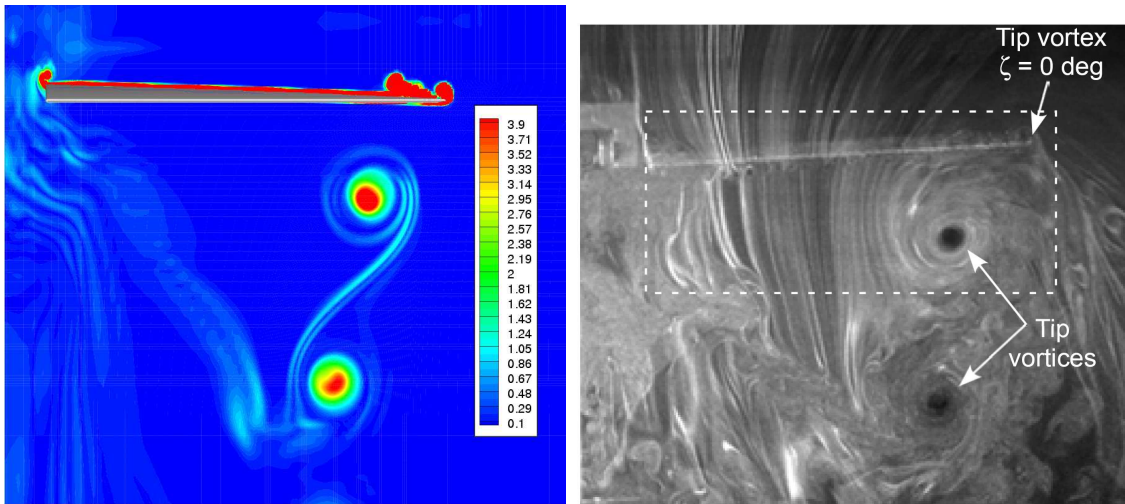


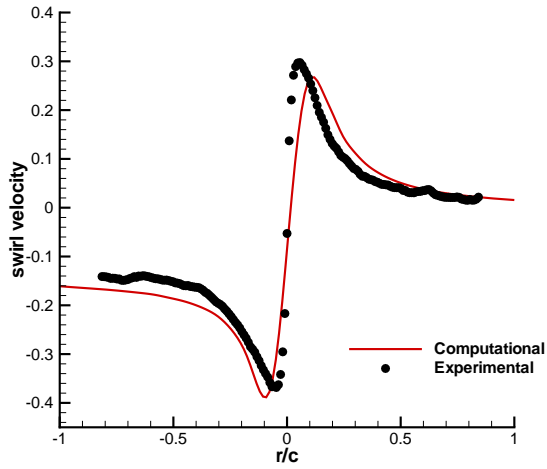
Figure 16: Experimental flow visualization (Ref. 23).



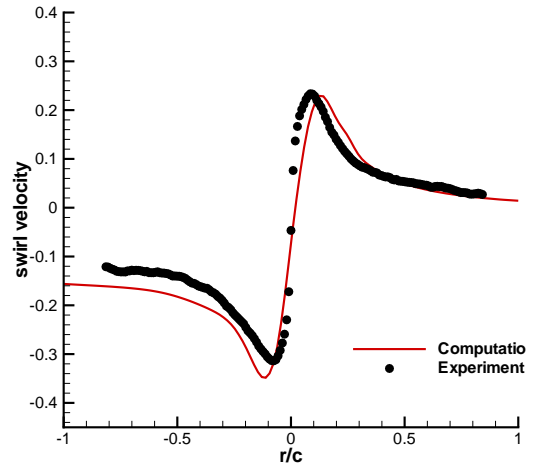
a) Contours of vorticity magnitude (normalized by tip speed and blade chord) at $\psi = 0^\circ$ for BLTE geometry at 12° collective setting.

b) Experimental flow visualization (Ref. 23).

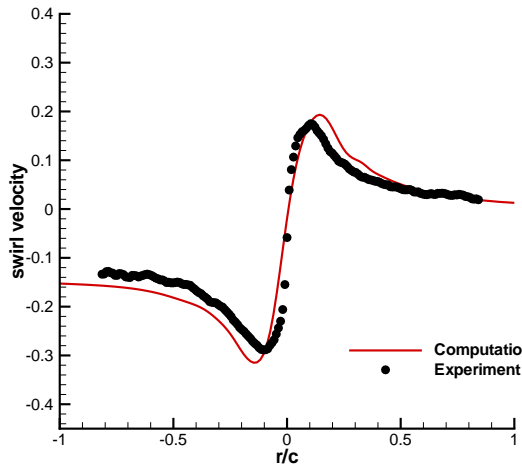
Figure 17: Flow-field comparison for micro-scale single rotor.



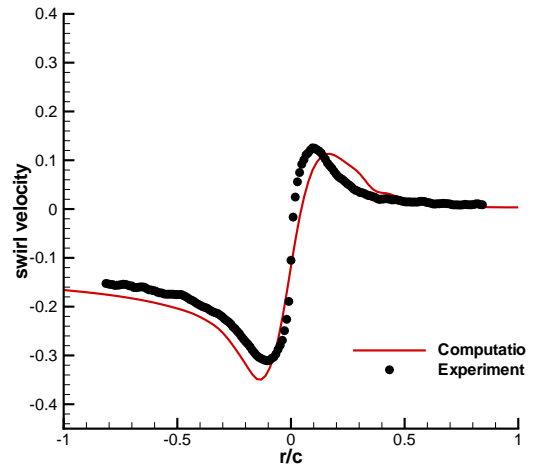
a) $\Psi = 30^\circ$



b) $\Psi = 60^\circ$

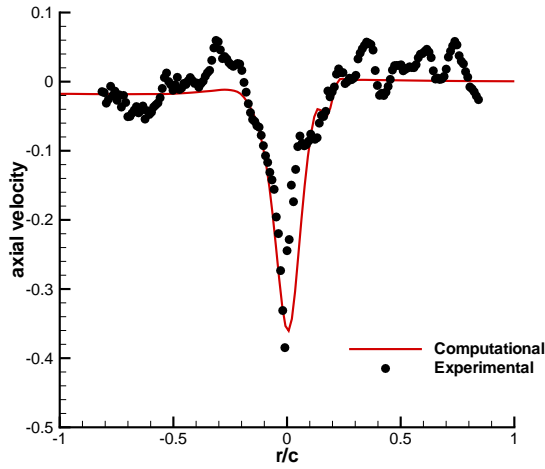


c) $\Psi = 90^\circ$

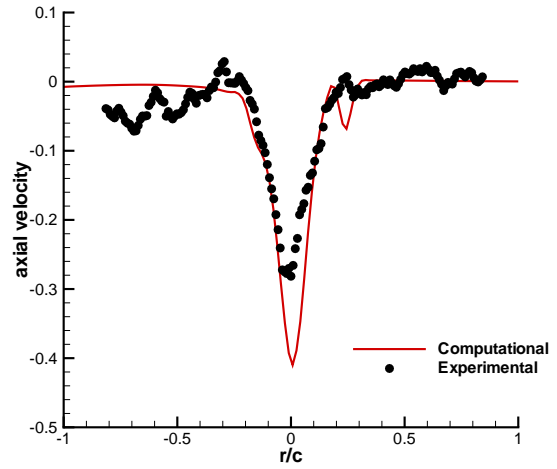


d) $\Psi = 180^\circ$

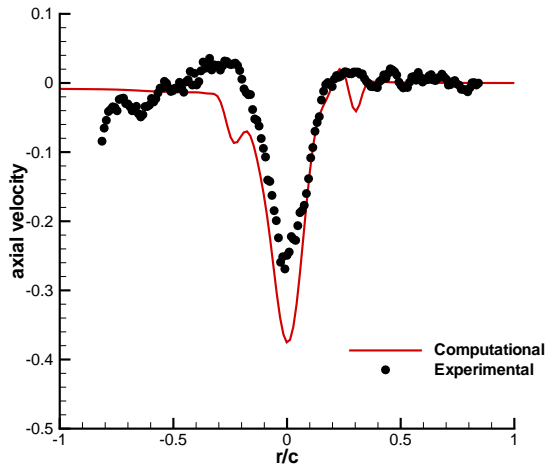
Figure 18: Vortex swirl velocity profile (non-dimensionalized by tip speed) comparison between computational BLTE geometry and experimental baseline geometry²³ of micro-scale single rotor, 12° collective setting.



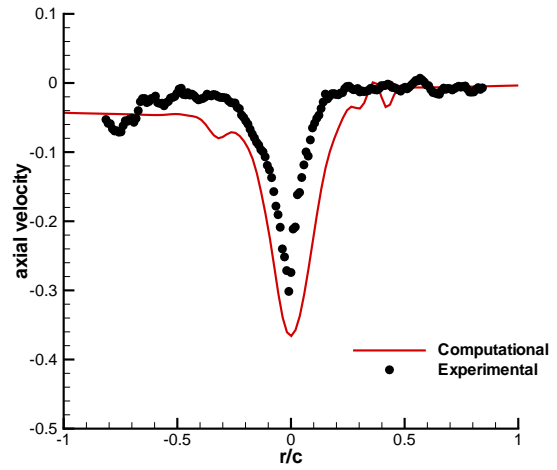
a) $\Psi = 30^\circ$



b) $\Psi = 60^\circ$

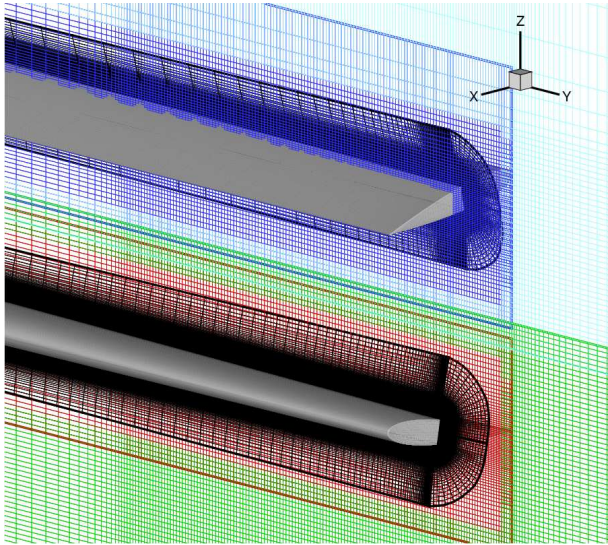


c) $\Psi = 90^\circ$

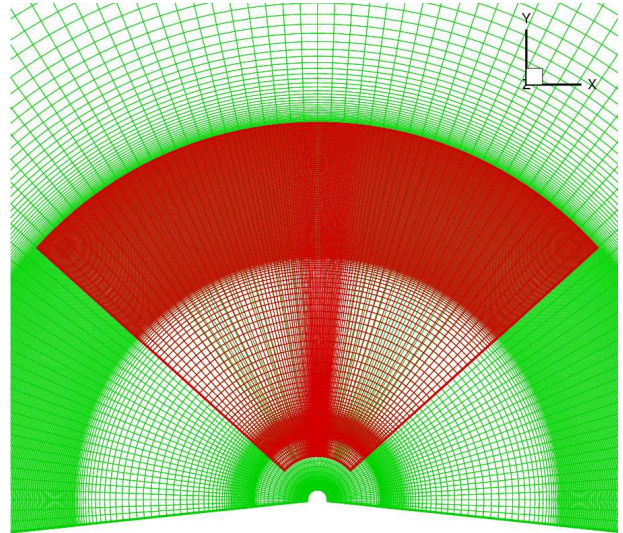


d) $\Psi = 180^\circ$

Figure 19: Vortex axial velocity profile (non-dimensionalized by tip speed) comparison between computational BLTE geometry and experimental baseline geometry²³ for micro-scale single rotor, 12° collective setting.

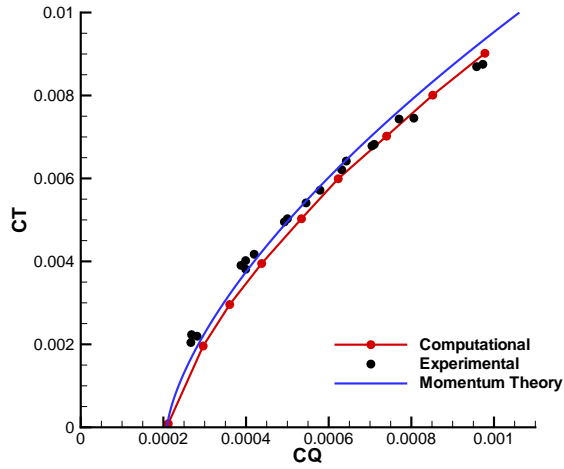


a) Blade meshes

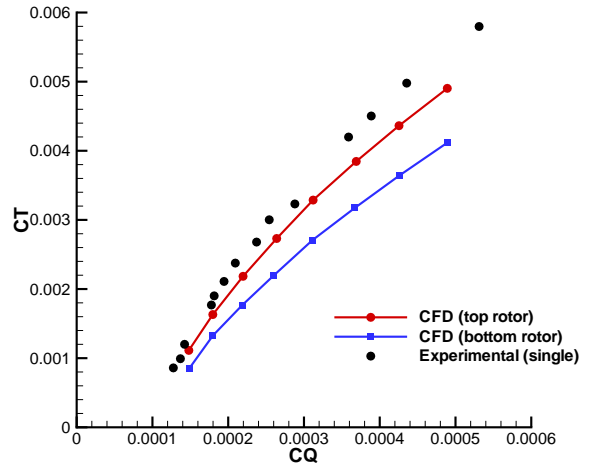


b) Cylindrical meshes with blade mesh boundaries

Figure 20: Computational mesh for full-scale coaxial rotor system.

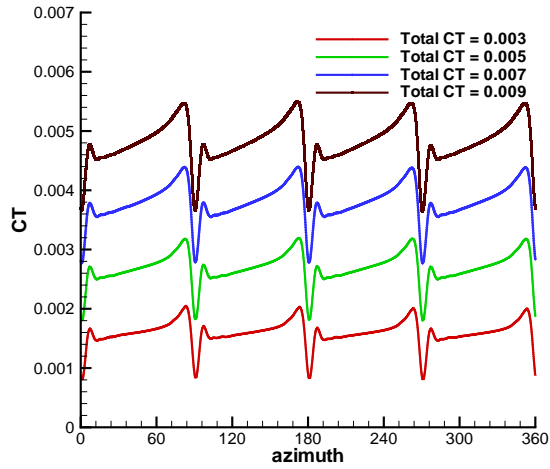


a) Total C_T (mean) versus total C_Q (mean)

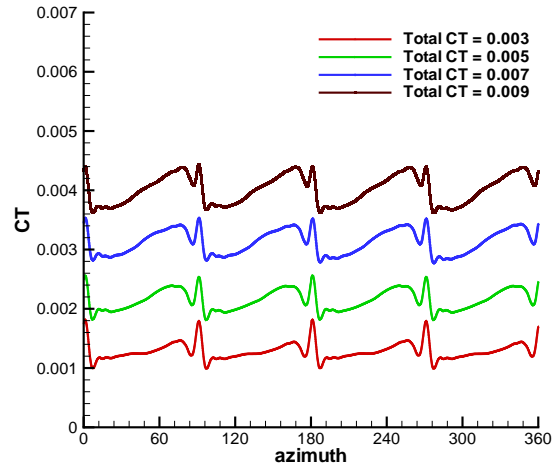


b) C_T (mean) versus C_Q (mean) for individual rotors.

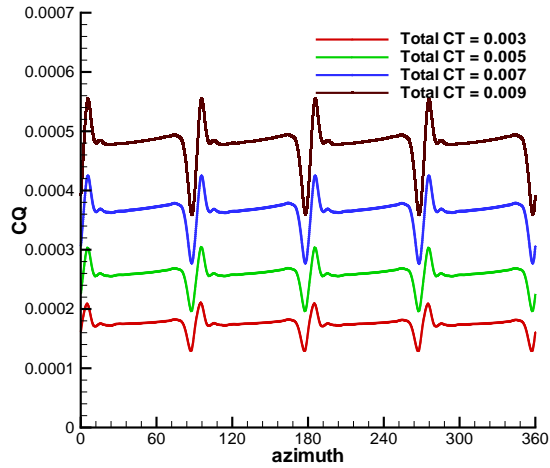
Figure 21: Comparison of performance with experimental data²⁵ for full-scale coaxial system.



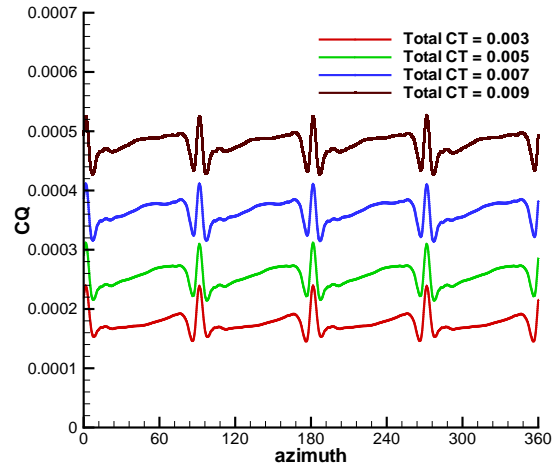
a) Top rotor C_T variation



b) Bottom rotor C_T variation

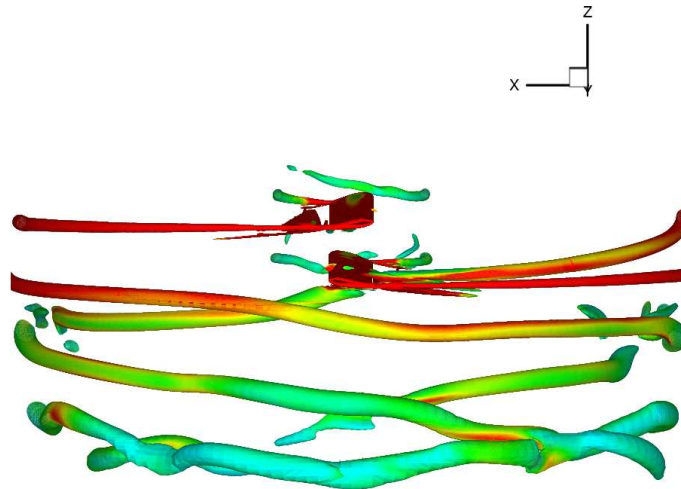


c) Top rotor C_Q variation



d) Bottom rotor C_Q variation

Figure 22: Temporal variation of C_T and C_Q for the top and bottom rotors over one revolution for various thrust levels for full-scale coaxial system.



a) $q = 0.025$

Figure 23: Iso-surfaces of the second invariant of the velocity gradient tensor colored by vorticity magnitude for full-scale coaxial system when the blades are aligned, case 7 ($C_T = 0.007$).

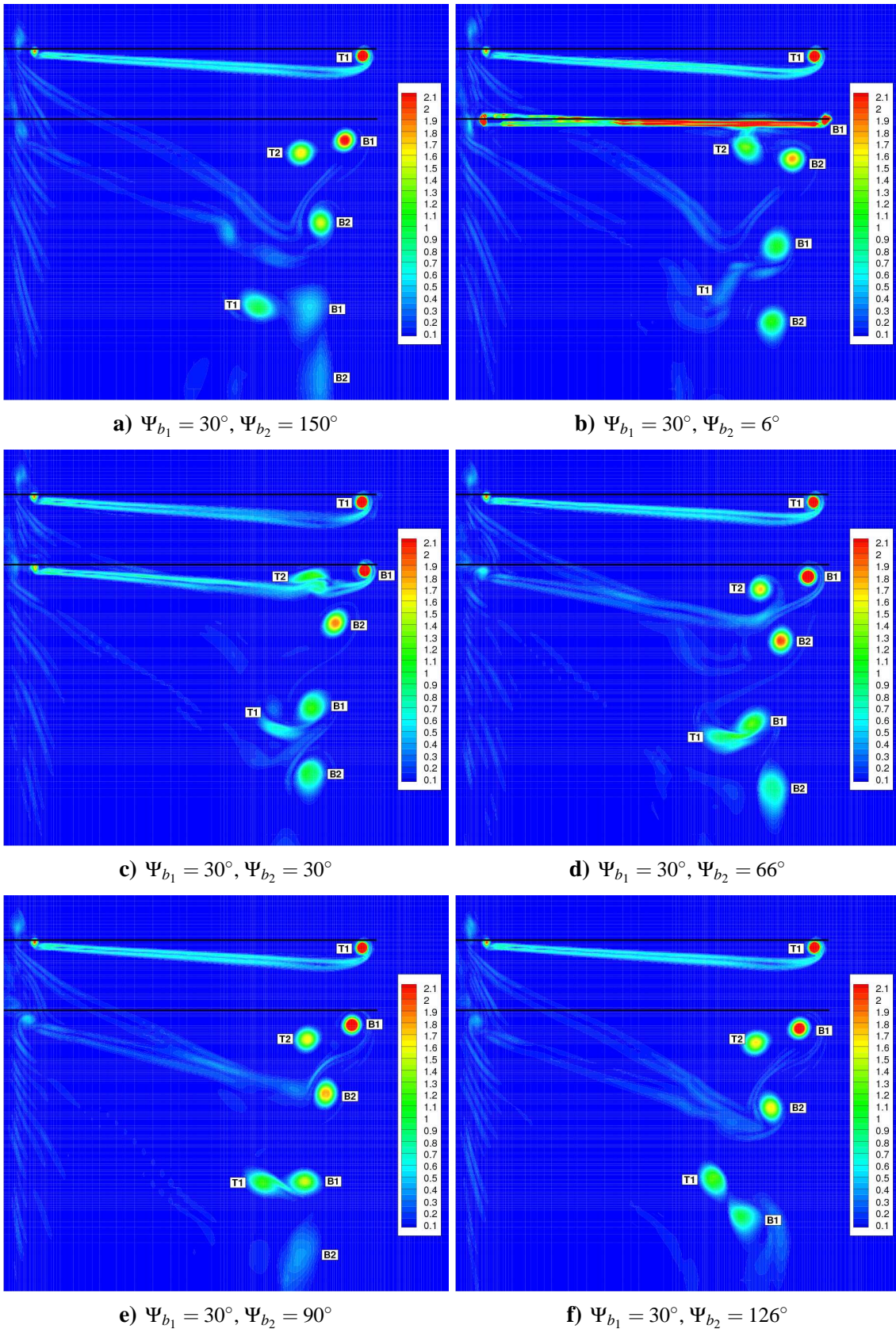
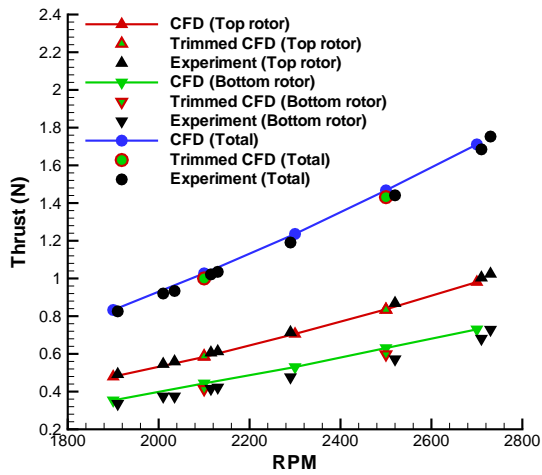
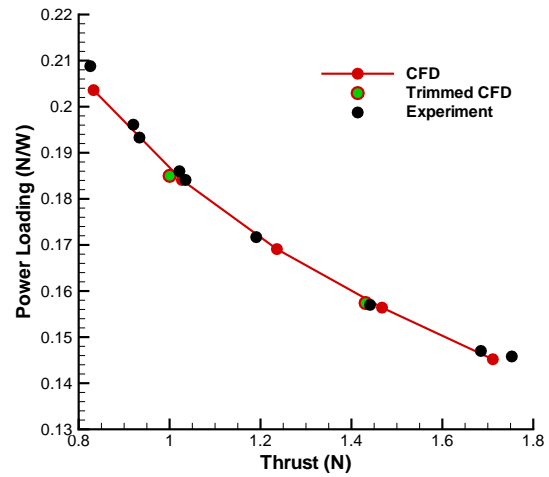


Figure 24: Vorticity magnitude contours (normalized by tip speed and blade chord) in a plane that is at 30° azimuth from the top rotor blade at different instances in time for full-scale coaxial system at $C_T = 0.007$.

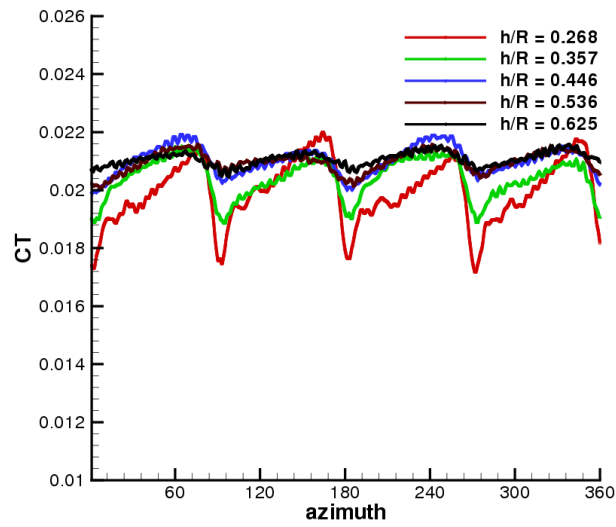


a) Thrust (mean) versus RPM

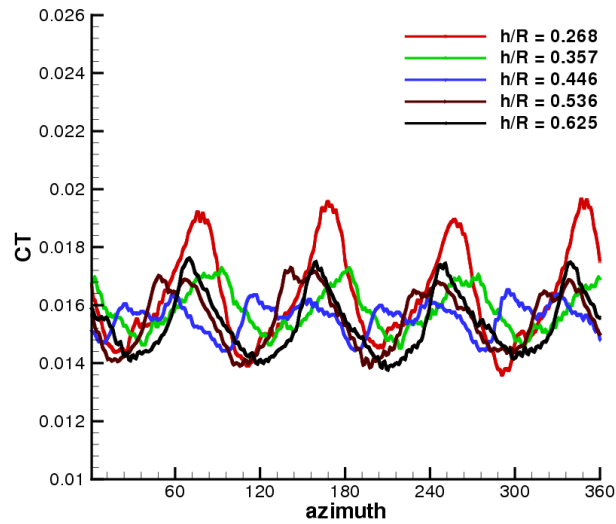


b) Power loading (mean) versus Thrust (mean)

Figure 25: Performance comparison with experimental data³⁰ at different RPM for micro-scale coaxial rotor.

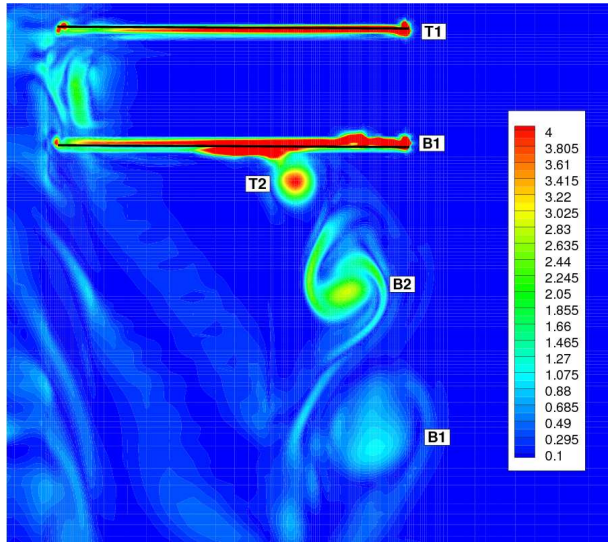


a) Top rotor C_T variation

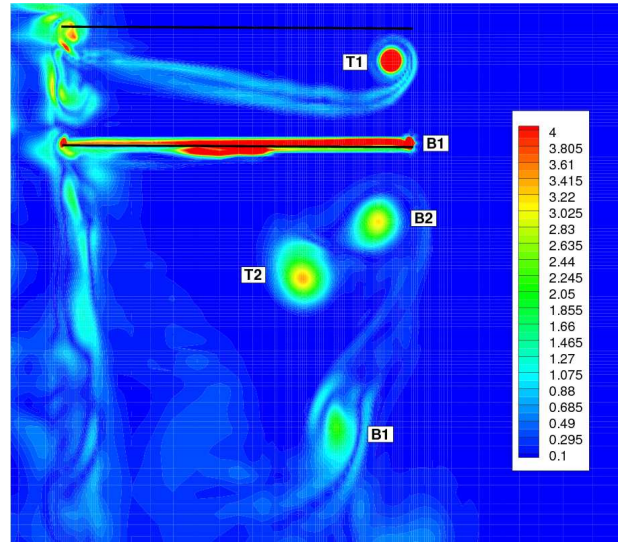


b) Bottom rotor C_T variation

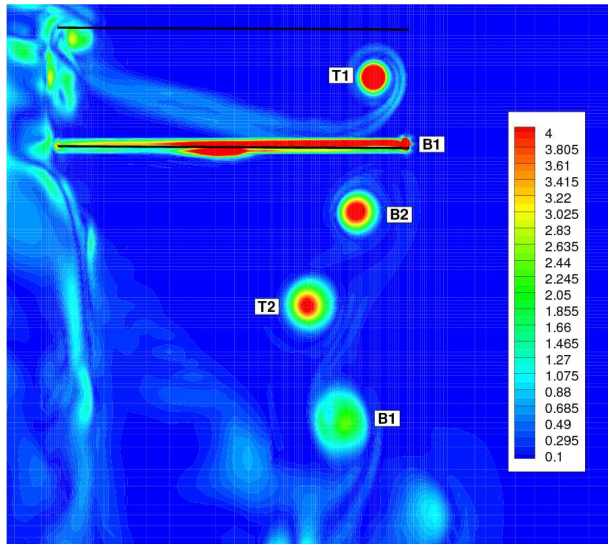
Figure 26: Temporal variation of C_T of the top and bottom rotors over one revolution for various rotor spacing for micro-scale coaxial system.



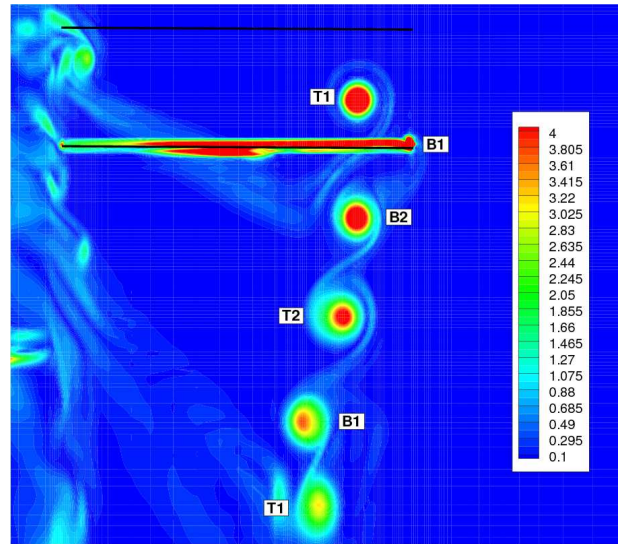
a) $\Psi_{b_1} = 0^\circ, \Psi_{b_2} = 0^\circ$



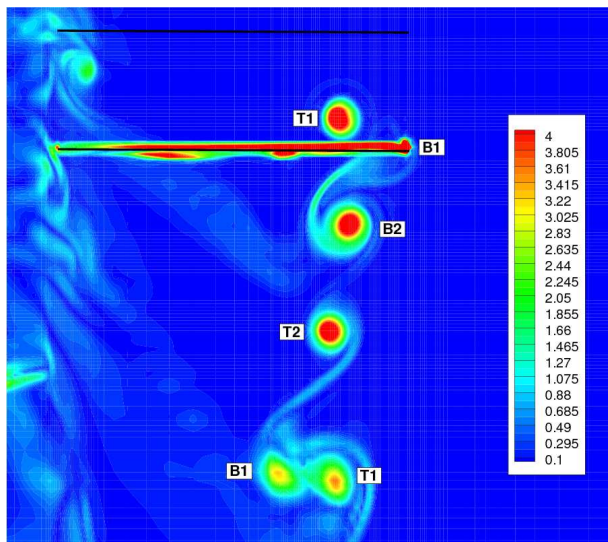
b) $\Psi_{b_1} = 36^\circ, \Psi_{b_2} = 0^\circ$



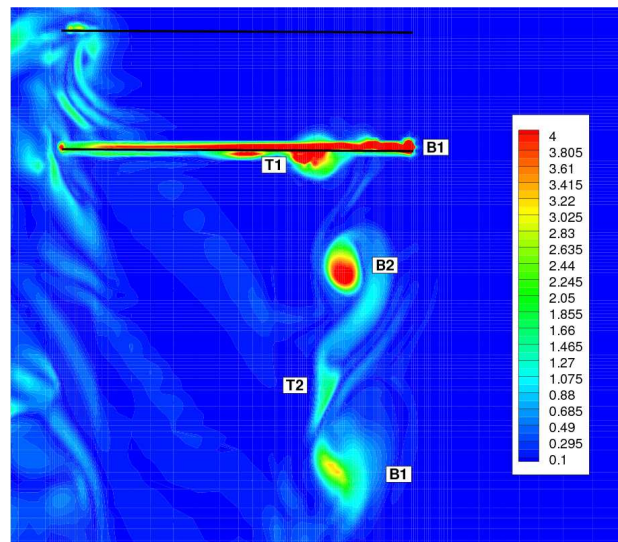
c) $\Psi_{b_1} = 60^\circ, \Psi_{b_2} = 0^\circ$



d) $\Psi_{b_1} = 96^\circ, \Psi_{b_2} = 0^\circ$



e) $\Psi_{b_1} = 120^\circ, \Psi_{b_2} = 0^\circ$



f) $\Psi_{b_1} = 156^\circ, \Psi_{b_2} = 0^\circ$

Figure 27: Vorticity magnitude contours in the plane of the bottom rotor blade at different instances in time for micro-scale coaxial system, $h/R = 0.268$.